

Answers to the numerical exercises:
Atmospheric boundary layer:
Integrating chemistry and land interactions

Jordi Vilà-Guerau de Arellano¹
Chiel C. van Heerwaarden²
Bart J. H. van Stratum²
Kees van den Dries¹

Published by:
Cambridge University Press

e-mail:
jordi.vila@wur.nl

¹Meteorology and Air Quality Section
Wageningen University
The Netherlands

²Max Planck Institute for Meteorology
Germany

October 13, 2015

Contents

1	Answers and discussion points hands-on exercises	5
2	Answers Chapter 4	7
3	Answers Chapter 5	11
4	Answers Chapter 6	15
5	Answers Chapter 7	21
6	Answers Chapter 8	25
7	Answers Chapter 10	31
8	Answers Chapter 12	35
9	Answers Chapter 13	39
10	Answers Chapter 14	45
11	Answers Chapter 15	49
	11.1 Section 15.2	49
	11.2 Section 15.5	51

1

Answers and discussion points hands-on exercises

This document contains the answers to the hands-on numerical exercises proposed in the book *Atmospheric Boundary layer: Integrating chemistry and land interactions*, plus supplementary information that will enable the reader to analyse the results of the numerical experiments in more detail. Note that CLASS offers the possibility of analysing several experiments and the evolution and relationships of a large number of variables. Although we restrict ourselves to the main questions posed by the hands-on exercises, we encourage readers to explore other processes and variables that they regard as relevant to their research interests. We therefore recommended that in some of the exercises the reader should make use of the numerical output of the experiment in addition to the figures plot with the graphical interface. We suggest to treat the data with an EXCEL spreadsheet or their own calculation and visualization software like python. In the answers and discussion points we mention equations, figures and tables employing the same numbers as in the book. The figures used in this document start with the acronym AN*, where the * is the specific number of the figure.

Besides the answers to the exercises, the CLASS web-link (classmodel.github.io) provides all the numerical settings of the hands-on exercises in order to ensure that all the numerical exercises proposed in the book can be reproduced. We will also appreciate if you contact us regarding potential improvements in the answers or extensions in the exercises (e-mail: jordi.vila@wur.nl).

2

Answers Chapter 4

- **Experiment 4.2.1.** Number and name experiments: 1) *mid-latitudes-nodiurnal*, 2) *desert-nodiurnal* and 3) *polar-nodiurnal*.

Note that we are now examining an academic case, where $(\overline{w'\theta'})_s$ is constant over time. In order to study the impact of the surface flux without including the diurnal variability effects. When performing a realistic case the diurnal cycle should be taken into account and $(\overline{w'\theta'})_s$ is not constant over time and under clear conditions it follows a sinusoidal evolution (see figure 4.1). The increase (decrease) in the kinematic potential temperature flux leads to an increase (decrease) in the potential temperature and boundary layer height and an increase (decrease) in the potential temperature jump at the boundary layer top. This increase (decrease) depends on the potential temperature lapse rate. Equations 4.2 and 4.5 in combination with 4.7 show that $\langle\theta\rangle$ and h are proportional to the surface sensible heat flux. It is important to notice that the increases(decreases) are non-linear: a doubling of $(\overline{w'\theta'})_s$ will not lead to a similar rise in the potential temperature and h .

- **Experiment 4.2.2.** Number and name experiments: 1) *encroachment-nodiurnal* and 2) *entrainment-nodiurnal*.

Compare the *ENCROACHMENT* case (entrainment of warm air is neglected, there is no jump in the potential temperature at the inversion) and the parameter β (Equation 4.7) with the *ENTRAINMENT* case. In the latter, the contribution of the entrainment of heat (negative value of the potential kinematic flux at the top of the boundary layer) leads to a deeper boundary layer and a slightly higher potential temperature. A modification of Equation 4.8 shows how the entrainment flux of heat w_e makes a positive contribution to the growth of the ABL:

$$\frac{\partial h}{\partial t} = \frac{1}{\gamma_\theta} \frac{\partial \langle\theta\rangle}{\partial t} = \frac{1}{\gamma_\theta} \left[\frac{(\overline{w'\theta'})_s}{h} + \frac{w_e \Delta\theta}{h} \right], \quad (\text{AN2.1})$$

where the last term of the right-hand-side is the contribution of the entrainment process. Note that the growth in potential temperature due to entrainment is relatively small. This is due to the positive and negative effects of entrainment. The positive input of warm air masses ($\frac{\partial \langle\theta\rangle}{\partial t} > 0$) is partially offset by the deeper ABL (h), *i.e.* heat has to be distributed throughout a larger volume.

- **Experiment 4.2.3.** Number and name experiments: 1) *weakinversion-nodiurnal* and 2) *stronginversion-nodiurnal*.

The effect of a stronger inversion at the top of the boundary layer leads to a delay in the growth of the ABL during the first hours of the numerical experiments. Note that this delay can last for several hours and that it is proportional to the strength of the potential temperature inversion. The best way of visualizing this process is to plot the temporal evolution of the potential temperature jump ($\Delta\theta$) and the vertical profiles of $\langle\theta\rangle$ (you can find both plotting options in GRAPH). It can be seen that in the case of strong inversion, the heat introduced at the surface is first employed to decrease $\Delta\theta$ to a value similar to that of the weak inversion case. After this time, the boundary layer growth and $\langle\theta\rangle$ -evolution follow a similar rate. In conclusion, the afternoon value of the boundary layer height retains a *memory* of the strength of the previous nocturnal ground inversion. Variables such as moisture or atmospheric constituents have larger values after sunrise when there is a stronger inversion, i.e. when the boundary layer growth is delayed and it remains shallow and almost constant on time.

- **Experiment 4.2.4.** Number and name experiments: 1) *control-nodiurnal*, 2) *highergamma-nodiurnal* and 3) *lowergamma-nodiurnal*.

This exercise complements the previous one in studying the role of prevailing conditions in the inversion and free troposphere in the development of a convective boundary layer. Figure AN2.1 a, b and c shows an example of respectively the temporal evolution of the boundary layer height, potential temperature and jump in potential temperature. For the sake of completeness, we show the vertical profiles of the potential temperature and buoyancy. These profiles are constructed as in Figure 2.7. Higher values of the free tropospheric potential temperature lapse rate (higher γ_θ) yield a slower growth rate of the boundary layer. This can be seen in Equation 4.6, where the $\Delta\theta$ rate is proportional to γ_θ and in Figure AN2.1a. As a result, in the case of high values of γ_θ , $\Delta\theta$ increases compared with the case of low values, as shown by Figures AN2.1c and AN2.1d. Notice, however, that the effect of the lapse rate of the potential temperature occurs at the end of the day, unlike the effect of $\Delta\theta$, which occurs in the earlier hours of the ABL development. We can then conclude that $\Delta\theta_0$ and γ_θ are related variables that act to prevent the growth of the boundary layer at different periods in its evolution.

To complete the discussion, in Figure AN2.1e we plot the potential temperature kinematic flux, which displays a linear decrease with height (see Box 3 for the full derivation of the linear heat flux). Notice that in the case of low values of γ_θ , the entrainment flux is located at a higher altitude, and its minimum value can be used as a criterion to define the depth of the ABL. It is also useful to check the value of the entrainment to the surface flux, since according to our closure assumption (Equation 4.7) needs to be equal to 0.2.

- **Experiment 4.2.5.** Number and name experiments: 1) *nosubsidence-nodiurnal* and 2) *subsidence-nodiurnal*

The inclusion of large-scale subsidence (Equation 4.4) suppresses the boundary layer growth. The values of the divergence of the mean horizontal wind ($\text{div}(\mathbf{U}_h)$ in BASIC window) used for the experiment range from 0 s^{-1} to $5.0 \cdot 10^{-5} \text{ s}^{-1}$. As a discussion point, it is important to be aware that the presence of subsidence inhibits boundary layer growth ($\frac{\partial h}{\partial t}$ becomes smaller); although the entrainment process is still present ($w_e \neq 0$). In order to reproduce a steady-state situation defined by $\frac{\partial h}{\partial t}=0$, we need to find initial equilibrium conditions by setting Equations 4.4 and 4.5 to zero. This gives us the following conditions for $\Delta\theta$ and w_s :

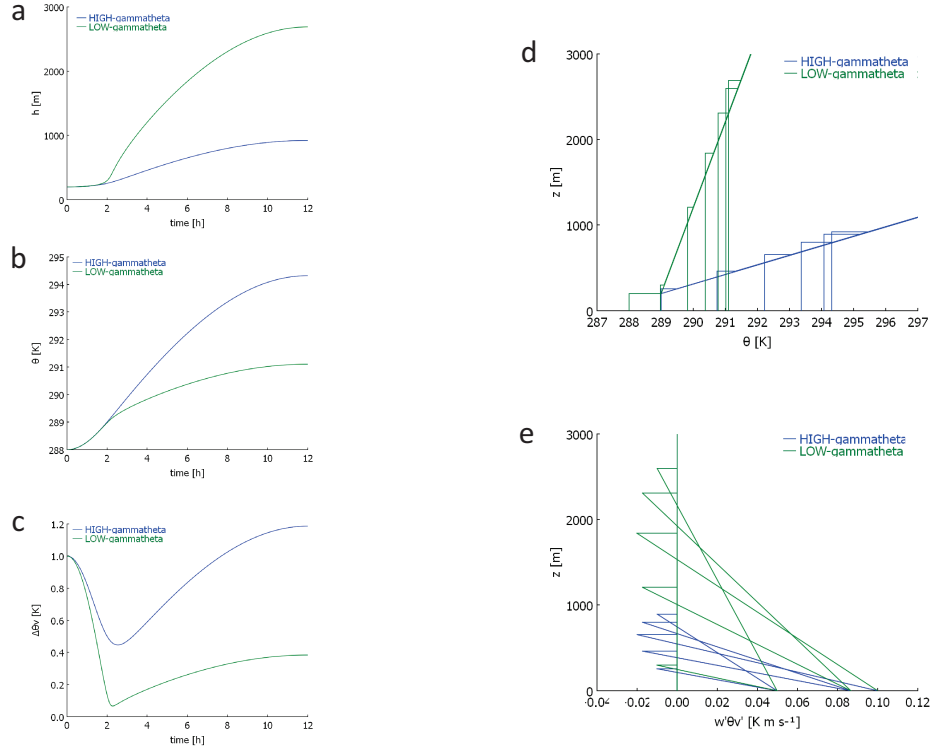


Figure AN2.1: Results of experiment 4.2.4. Temporal evolution of boundary layer height (a), mixed-layer potential temperature (b) and jump in potential temperature (c). Vertical profiles (at two-hour frequency intervals) of the potential temperature and buoyancy (in this experiment equal to the flux of the potential temperature (option Vertical Profiles in GRAPH)). The experiments correspond to the BASIC setting, with the following values for γ_θ : 0.001 K m^{-1} (LOW) and 0.009 K m^{-1} (HIGH).

$$\Delta\theta = \frac{\beta \gamma_\theta h}{1 + \beta} \quad (\text{AN2.2})$$

$$w_s = - \frac{(1 + \beta) \overline{(w'\theta')}_s}{\gamma_\theta h}. \quad (\text{AN2.3})$$

To test the validity of these expressions the reader can try different values of γ_θ , h and β , and check whether an equilibrium for h is reached. Note that these exercises need to be done with constant sensible heat flux (no daily cycle). Note also that the value prescribed is the divergence of the mean horizontal wind (Equation 4.4), and therefore $\omega_{1s} = -(w_s/h)$. As an example, we have calculated $\Delta\theta$ and w_s for the following values: $\gamma_\theta = 0.006 \text{ K m}^{-1}$, $h = 2000 \text{ m}$ and $\overline{(w'\theta')}_s = 0.1 \text{ K m s}^{-1}$. The equilibrium values are: $\Delta\theta = 2 \text{ K}$ and $w_s = -0.01 \text{ m s}^{-1}$ (div $(U_h) = 5.0 \cdot 10^{-6} \text{ s}^{-1}$).

- **Experiment 4.2.6.** A surface heat flux with diurnal variability represents a realistic case. By introducing a diurnal variability of the surface heat flux $\overline{(w'\theta')}_s$ less heat is introduced in the system. As a result, the boundary layer grows more slowly and the potential temperature and h-temporal evolution reaches a lower maximum value. As mentioned and expected, using

the diurnal cycle option, the variability of potential temperature and boundary layer height follows a more realistic pattern. Note also that in the experiment with stronger inversion, it takes longer to break the inversion, since the heat introduced by the surface sensible heat flux is less during the morning hours. This can be visualised by plotting the vertical profiles of the potential temperature.

3

Answers Chapter 5

- **Experiment 5.3.1.** Number and name experiments: 1) *control*, 2) *desert* and 3) *precipitation*.
Again, we are examining an academic case where $(\overline{w'\theta'_v})_s$ is constant over time. Increasing the surface moisture flux enhances the specific moisture (Equation 5.1), but it also affects the boundary layer dynamics. This can be seen by the equation of boundary layer growth, which is now governed by the buoyancy and the jump in virtual potential temperature θ_v . The equation reads:

$$\frac{\partial h}{\partial t} = -\frac{(\overline{w'\theta'_v})_e}{\Delta\theta_{vh}} + w_s = \frac{\beta (\overline{w'\theta'_v})_s}{\Delta\theta_{vh}} + w_s. \quad (\text{AN3.1})$$

An increase in $(\overline{w'q'})_s$ leads to an increase in the buoyancy flux as defined by Equation 5.5. As the boundary layer growth equation (Equation AN3.1) shows, h is inversely proportional to $\Delta\theta_{vh}$. Larger negative changes in the jump in specific moisture values lead to a drop in the virtual potential temperature jump (Equation 5.7) that favours boundary layer growth (Equation AN3.1). The physical explanation is that the drier air in the free atmosphere is more dense than wetter air, and as a result, the parcels that have originated at the boundary layer are more buoyant in the drier environmental free atmosphere than under wetter free atmospheric conditions. Therefore, parcels make a large positive difference in potential temperature (they are more buoyant) and can penetrate deeper into the inversion. In our modelling framework this is represented by the virtual potential temperature jump. In other words, under equal initial and boundary conditions, a drier FT is represented by a larger (more negative) Δq . In the current experiment, larger $(\overline{w'q'})_s$ yields to larger negative Δq -jumps and thus lower $\Delta\theta_v$ values. Therefore, $\Delta\theta_v$ can also be interpreted as a density difference (including the temperature and moisture effects) between the ABL and FT conditions. Lower $\Delta\theta_v$ show larger differences (for instance drier air in the FT) and therefore more potential for the parcel to move upwards. Note that lower values of $\Delta\theta_v$ physically means weaker inversion.

With respect to the cloud formation, we first need to define the two criteria employed here in order to determine the cloud formation: (i) $h > \text{LCL}$ (parcels are able to reach saturation within the ABL) and (ii) $\text{RH}_{\text{top}} = 100\%$. As Figure 5.2 shows, $(\overline{w'q'})_s$ tends to decrease the height of LCL (positive effect for boundary-layer cloud formation) but also increases the h (negative effect for cloud formation). In order to determine which effect is dominant, it is therefore convenient to visualise h and LCL in the same figure (use an EXCEL spreadsheet or your own visualization software). As an alternative, we can plot RH_{top} . In this case, we

found that under conditions of wetter soil (numerical experiment precipitation), boundary layer clouds will be formed earlier than under drier soil condition, *i.e.* a relative humidity of 100 is reached earlier. For a more complete understanding of the formation of clouds, we recommend performing and analysing the exercise 15.6 in Chapter 15.

- **Experiment 5.3.2.** Number and name experiments: 1) *control*, 2) *wet* and 3) *dry*.

As in the previous exercise, a drier free atmosphere (or residual layer) promotes the boundary layer growth by reducing the jump in virtual potential temperature, thus reducing the strength of the inversion. Figure AN3.1 shows the results of the experiment and the evolution of the boundary layer height, the jump in virtual potential temperature and the relative humidity at the top for three numerical experiments characterized by different values of Δq . The main difference with respect to the previous case is that the drying in the case where $\Delta q = -5 \text{ g}_w \text{ kg}_a^{-1}$ lowers the specific moisture values. As a result, the lifting condensation level rises, while the relative humidity at the top of the ABL falls (see Figure AN3.1c).

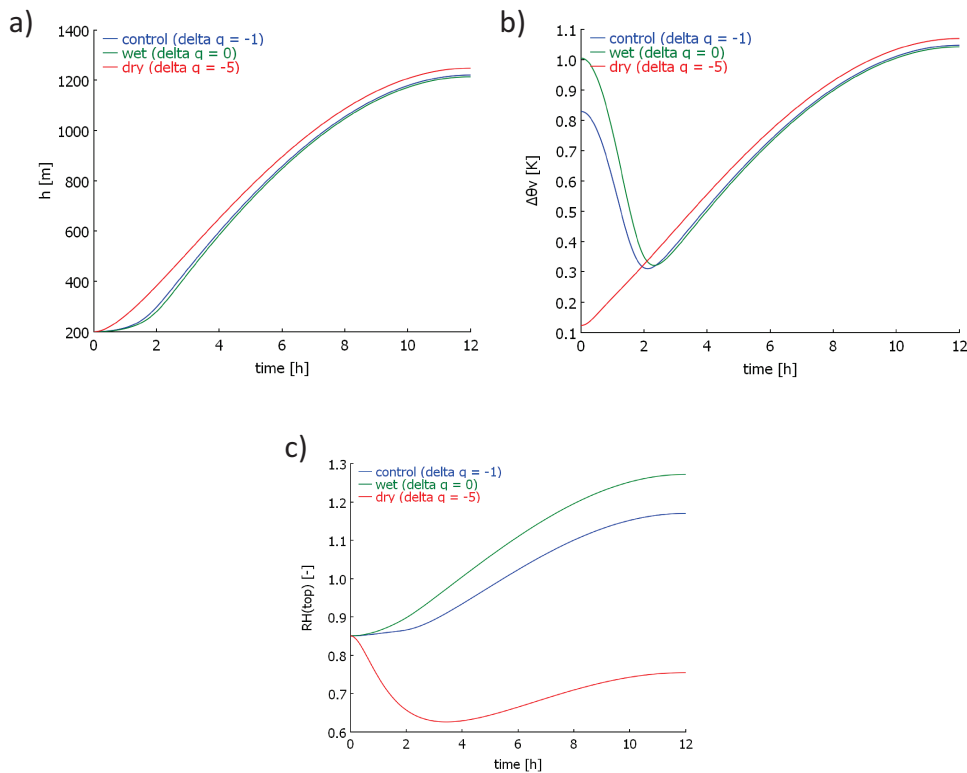


Figure AN3.1: Results of experiment 5.3.2. Temporal evolution of the (a) boundary layer height, (b) jump in the virtual potential temperature and (c) relative humidity at the top of the boundary layer for the cases: $\Delta q = -1 \text{ gr kg}^{-1}$, 0 gr kg^{-1} and -5 gr kg^{-1} .

- **Experiment 5.3.3.** Number and name experiments: 1) *control*, 2) *wet* and 3) *dry*.

Positive(negative) values of γ_q lead to an increase (decrease) in the specific moisture. This has consequences for the development of the boundary layer. A drier free atmosphere (experiment DRY with negative value of γ_q) results in a rise in the negative value of Δq and therefore a fall in the value of the virtual potential temperature jump. As Equation AN3.1 shows, this will lead to a deeper ABL. With respect to cloud formation, drying leads to a delay in the onset of boundary layer clouds that can be seen by the crossing of the line $RH_{\text{top}}=1$ is

later in the DRY than in the CONTROL and WET experiments.

- **Experiment 5.3.4.** Number and name experiments: 1) *control* and 2) *sea breeze*.

Depending on the sign of the advection of the moisture, the impact on the boundary layer dynamics will be different. Focusing on a case with positive advection (SEA BREEZE) ($q_{adv} = 0.54 \text{ kg}_w \text{ kg}_a^{-1} \text{ hr}^{-1}$ or $0.00015 \text{ g}_w \text{ kg}_a^{-1} \text{ s}^{-1}$) and therefore moistening of the ABL), the entrance of air masses with high water content leads to a rise in specific humidity and therefore to a fall in the negative value of the specific humidity jump (Δq becomes more negative). As a result, $\Delta\theta_v \downarrow$ leads to a growth in the ABL for the SEABREEZE case. Boundary layer clouds are also favoured by the advection of moist air. An opposite effect will be found if the advection of air transports air masses characterized by drier air. In order to complete the analysis of the effect of the sea breeze, we recommend performing the numerical experiments suggested in section 13.1 including the interaction with land surface processes (Chapter 13).

4

Answers Chapter 6

- **Experiment 6.4.1.** Number and name experiments: 1) *control*, 2) *higherUg* and 3) *lowerUg*.

In order to follow a logical order in analyzing our results, we first check whether the boundary layer height, mixed-layer potential temperature and specific humidity are different in the three experiments. Since the physical parameterization to introduce the effect of mechanical turbulence (shear effect) is disabled, the boundary layer height and budget of potential temperature and specific humidity must be equal for the three experiments.

As Equation 6.12 and 6.13 shows, a larger geostrophic wind U_g leads to a rise in the V -component. Acceleration is caused due to the larger U_g imply larger horizontal pressure gradients (second term right hand side in Equation 6.13). In turn, there is also a deceleration in the flow due to the increase (negative value) in the Coriolis term, term $-f_c < U >$, which increases due to the rise in $f_c < V >$ in Equation 6.12.

In the specific case under study, with a V_g equal to 0 (see Table 6.1), this leads to the term $-f_c (V_g - \langle V \rangle)$ also becoming positive, leading in turn to $\frac{\partial \langle U \rangle}{\partial t} > 0$. The physical explanation is that under identical growth of the boundary layer (notice that h has the same evolution in the three numerical experiments), the experiment with a prescribed highest U_g results with the highest velocity within the ABL. This is due to the air entrained in the ABL moves more rapidly (more accelerated air masses in the free troposphere). With regard to friction velocity, we find that a higher U_g also results in higher gradients near the surface and that as a result, the mechanical turbulence increases. As the values of the stability parameters Ri_b and L (Equation 6.6 and 6.7) show, the ABL flow becomes closer to a neutral atmospheric stabilization for the numerical experiments control and higherUg. For the numerical experiment lowerUg, convective turbulence (buoyancy effects) becomes similar in order of magnitude to mechanical turbulence driven by wind and therefore the values of L and Ri_b become more negative.

- **Experiment 6.4.2.** Number and name experiments: 1) *mid-latitudes*, 2) *polar* and 3) *tropical*.

Three additional experiments with a long duration (60 hours).

The value of the Coriolis effect controls the inertial oscillation (IO) of the $\langle U \rangle$ and $\langle V \rangle$ components of the ABL. Here, we understand IO as the oscillation of the ABL wind components with respect the U_g and V_g components. The latter are in equilibrium. Deviations of $\langle U \rangle$ and $\langle V \rangle$ from this equilibrium generates an oscillation around U_g and V_g . IO is similar to the oscillation produced by a spring. As [Schröter et al \(2013\)](#) points out and as is explained in the theoretical section of Chapter 6, surface resistance and entrainment of momentum damp such oscillations.

Larger values of $f_c=1.5 \cdot 10^{-4} \text{ s}^{-1}$ (POLAR experiment) increase the frequency of the oscillations.

To better visualize this effect, we recommend plotting, in addition to their temporal evolution, the $\langle U \rangle$ component against the $\langle V \rangle$ component. Integration over 60 hours shows more clearly their complete oscillations and the dependence on the value of the Coriolis effect quantified by the Coriolis parameter f . Figure AN4.1 shows the temporal evolution of the V component and the inertial oscillation for the numerical experiments integrated over 60 hours. For a more complete description and explanation of the IO, see experiment 6.5.8.

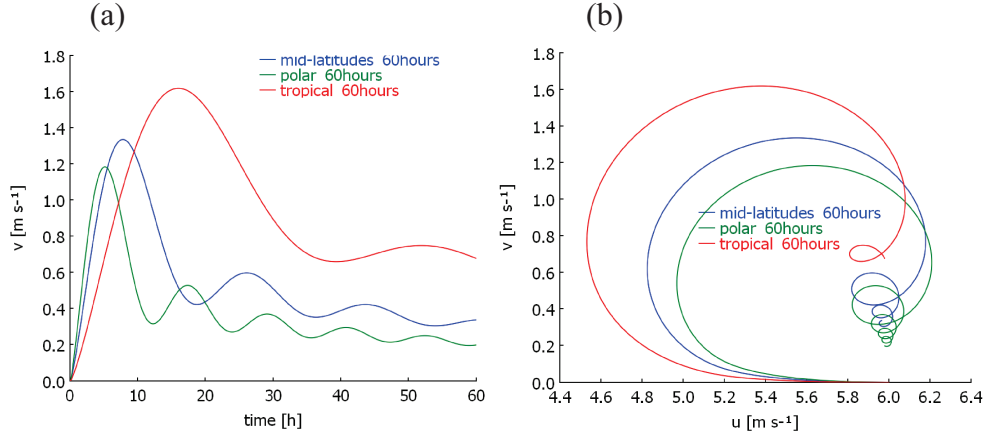


Figure AN4.1: Results of experiment 6.5.2: (a) time evolution of the V -component and (b) oscillation of the U and V components. The numerical experiments refer to three cases with different values of f_c . The period of integration is 60 hours.

- **Experiment 6.4.3.** Number and name experiments: 1) *control*, 2) *control-noSL* and 3) *control-higherzo*.

By switching on the atmospheric surface layer representation (Equation 6.3) and introducing a better physical representation that includes the atmospheric surface layer u_* , (see Figure 6.1) we obtain a smoother transition between the mixed layer values of the velocity components and the boundary layer values at the surface ($\langle U \rangle_o = \langle V \rangle_o = 0 \text{ m s}^{-1}$), while the friction velocity is calculated explicitly as a function of roughness length (Equation 6.4). In the experiments under analysis and with higher z_o , this leads to a larger u_* and therefore to a higher removal rate of the U component due to the larger friction. In other words, momentum is extracted from the ABL that causes the wind to decelerate.

- **Experiment 6.4.4.** Number and name experiments: 1) *control*, 2) *control-higherjump* and 3) *control-lowerjump*.

The difference between the geostrophic wind and the wind in the ABL influences the values of the wind through the entrainment of momentum, as expressed by the relationship:

$$\overline{(w'u')}_e = -w_e \Delta U, \quad (\text{AN4.1})$$

where w_e is the entrainment velocity and ΔU is the difference between the geostrophic wind and the the wind in the ABL. Positive values of ΔU (higher geostrophic winds) lead to wind entrainment with higher momentum (acceleration), with the result that the U component of the wind velocity increases. In spite of the increase of U (that represents $\frac{\partial V}{\partial t} < 0$, see Equation 6.13), the large value of the U_g components is still dominant (in the case of numerical experiment *control-higherjump*) and brings about an increase in the V -component. We recommend

performing a sensitivity analysis that assigns different values to U_g and V_g to study how $\frac{\partial \langle U \rangle}{\partial t}$ and $\frac{\partial \langle V \rangle}{\partial t}$ vary according to the values of U_g and V_g . An opposite effect, deceleration of the flow, is found if the velocity of the geostrophic effect is lower than the wind in the ABL (negative velocity jump).

- **Experiment 6.4.5.** Number and name experiments: 1) *control* and 2) *control-baroclinicity*.
The increase in the wind speed with height in the free troposphere (baroclinicity) characterized by a lapse rate for momentum γ_u larger than 0 also accelerates the wind in the ABL as expressed by the evolution of the jump of U at the entrainment zone (Equation 6.17). In our experiments we have imposed a positive gradient on the U component equal to $1 \cdot 10^{-3} \text{ s}^{-1}$. Note that the effect of baroclinicity in the evolution of the wind speed becomes larger over time, since at higher altitudes the wind speed is larger (similar effect as exercise 4.2.4).
- **Experiment 6.4.6.** Number and name experiments: 1) *control* and 2) *control-advectionU*.
As in the two previous exercises a positive (negative) advection of momentum results in an acceleration of the flow and an increase (decrease) in the U component. It is important to notice that for the case with a positive jump of ΔU , positive momentum advection will reduce the jump of U at the inversion that reduces the entrainment of air with higher momentum, and therefore could counteract to a certain extent the acceleration of the flow within the ABL.
- **Experiment 6.4.7.** Number and name experiments: 1) *control*, 2) *control-sheareffectwe* and 3) *control-sheareffectwe-hz0*.
In our modelling framework, wind only influences boundary layer dynamics by taking into account the extra contribution of the mechanical turbulence in the equation that governs ABL growth (last term on the right hand side of Equation 6.20). This is therefore the only set of numerical experiments in which the boundary layer height and the budgets of heat and specific humidity are affected by the wind characteristics. As these equations show, larger values of u_* yield larger ABL growth and therefore larger entrainment velocity. By visualising the evolution of h , $\langle \theta \rangle$ and $\langle q \rangle$ we find that higher values of u_* increase h and the potential temperature but reduce specific humidity due to the larger entrainment of drier air. We recommend performing a sensitivity analysis, using different settings of initial (U_o, V_o, \dots) and boundary conditions (z_o, \dots) to study the effect of friction velocity on ABL growth. For example, a larger value of z_o will lead to a larger value of u_* and therefore to an increase in the effect of mechanical turbulence on the boundary layer dynamics.
- **Experiment 6.4.8.**
 - a. Number and name experiments: 1) *NG-nozo*, 2) *NG-lowz0* and 3) *NG-highzo*.
Figure AN4.2 shows the results of the numerical experiments that analyze the behaviour of wind under different conditions of roughness length (surface friction). In Figure AN4.2a, we show the damping effects caused by the surface friction due to the changes in the roughness length. In the experiment with higher z_o , the U component of the velocity is rapidly damped, whereas in the experiment in which there is virtually no z_o , the oscillation remains, albeit somewhat damped, for the whole integration period. This effect is better visualized in the trajectories (Figure AN4.2b, and here we recommend to change the x and y -axis to 0 and 8 ms^{-1} as done in the figure), where in the case *NG-nozo*, the damping is minimal (see the zoom-in of Figure AN4.2c), compared with the other two experiments (see Figure AN4.2d). In Figure AN4.2b, we manually draw part of the circle of equilibrium (Schröter et al (2013)) that links the frictionless regime

to the infinite friction. As the circle of equilibrium (CEV) line shows, this equilibrium moves on a circular line from $(|U_g|, 0)$ and $(0, 0)$ with its center at $(|U_g|/2, 0)$.

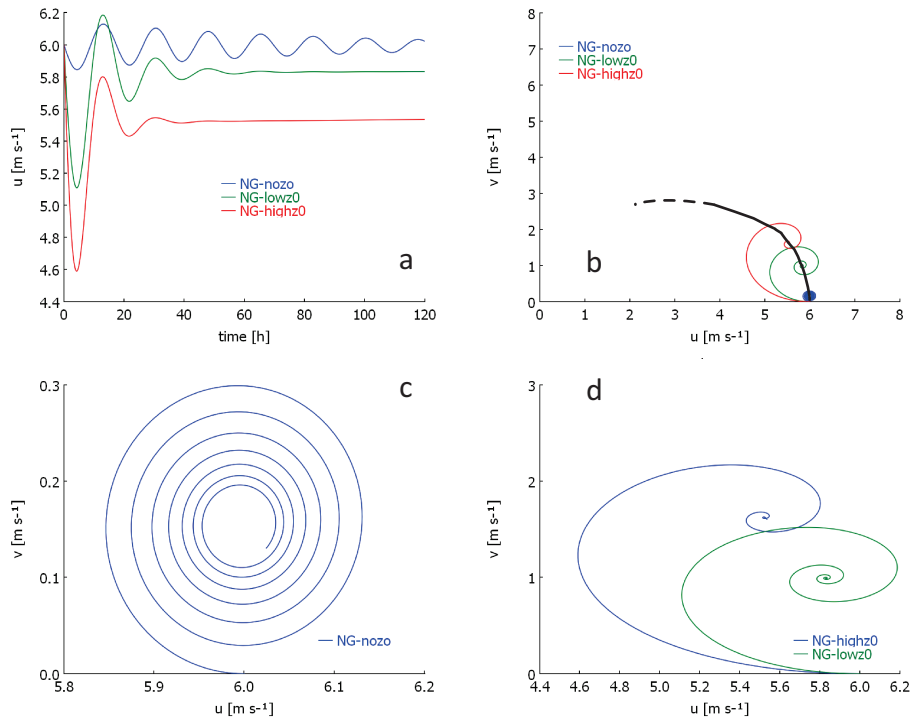


Figure AN4.2: Results of experiment 6.5.8a:(a) Temporal evolution of the U component ;(b) oscillation of the U and V components (trajectories) for the three experiments including the circle of equilibrium ;(c) zoom in the oscillation with a very low roughness length $z_0=1.10^{-8}$ m (experiment NG-nozo) (frictionless regime) and (d) zoom in the experiments NG-lowz0 $z_0=1.10^{-2}$ m and NG-highz0 $z_0=1.10^{-1}$ m.

b. Number and name experiments: 1) NG, 2) NG-U3 and 3) NG-U2.

Figure AN4.3b shows the trajectories for the three experiments initialized with different $\langle U \rangle$. In the cases in which the wind is initialized with different values from 6 m s^{-1} , we find the oscillation of the wind vector on a circle around the value of the geostrophic wind, in this case, 6 m s^{-1} .

c. Number and name experiments: 1) SF+EN.

Figure AN4.4 shows the temporal evolution of the U-component and the trajectories of the $\langle U \rangle$ - and $\langle V \rangle$ -components in the case of the growing ABL. Notice that entrainment of momentum act as an additional damping effect of the wind oscillation. The combined effect of surface friction and entrainment leads to the formation of a twisted spiral of the U – V trajectory as shown in Figure AN4.4b.

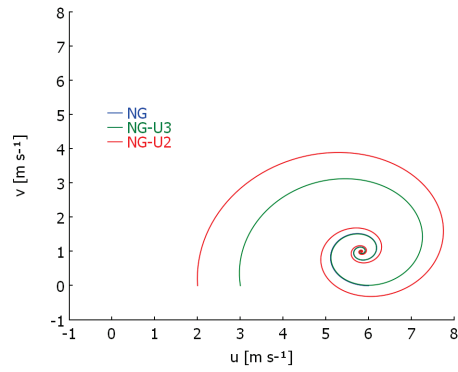


Figure AN4.3: Results of experiment 6.5.8b: Oscillation of the U and V components (trajectories) for the three experiments $\langle U \rangle_0 = 6 \text{ m s}^{-1}$ (NG), $\langle U \rangle_0 = 3 \text{ m s}^{-1}$ (NG-U3) and $\langle U \rangle_0 = 2 \text{ m s}^{-1}$ (NG-U2).

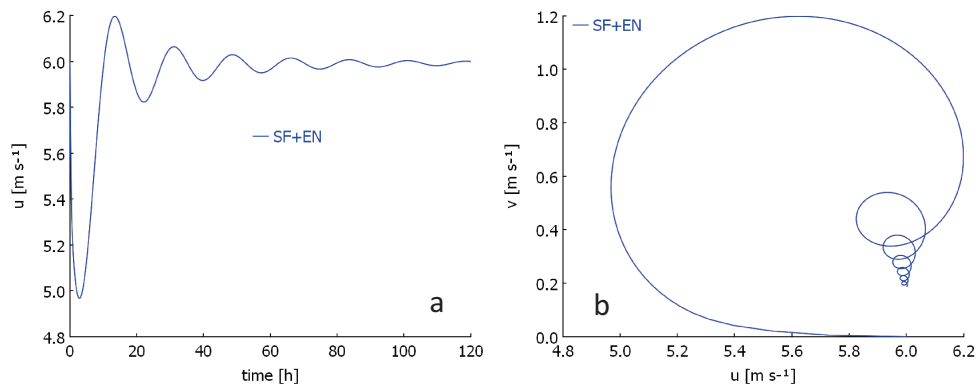


Figure AN4.4: Results of experiment 6.5.8c: (a) Temporal evolution of the U component; (b) oscillation of the U and V components for the experiment with growing ABL (surface friction and entrainment regime).

5

Answers Chapter 7

- **Experiment 7.3.1.** Number and name experiments: 1) *bottom-up* and 2) *top-down*.

We study the dependence of the temporal evolution of an inert scalar whether it is introduced as a surface emission (*bottom-up* experiment) or is entrained from the free troposphere (*top-down*) (see Figure 7.2). In the tab Wind initial and boundary conditions can be prescribed. It is important to first ensure that the surface and entrained fluxes are equal at the beginning of the experiment. In both cases, we study a situation in which the scalar is introduced in the ABL, but either at the surface (*bottom-up*) or at the entrainment zone (*top-down*). As a result, the surface flux is positive and the entrainment flux is negative, indicating transport of air masses from the free troposphere into the ABL. Note that the scalar at the free troposphere has a larger mixing ratio than in the ABL and as a result a positive jump, i.e. negative entrainment flux.

When we compare the two experiments, the results of $\langle s \rangle$ show that in the *top-down* experiment the scalar mixing rate is higher, due to the efficiency of the entrainment process in introducing the free troposphere scalar. Note that during the first two hours of the experiment, the entrainment velocity w_e and the jump in the scalar Δs have larger values (plot both quantities to visualise these). At the end of both experiments, we find almost similar values of the scalar mixing ratio, due to the fact that we prescribe similar surface and entrainment fluxes at the initial time. If we continue the experiments for a longer period of time, the entrainment flux becomes zero since $\Delta s \rightarrow 0$ (this is only the case for the *top-down* experiment).

To complete this exercise, it is worth repeating the experiment for different initial values of the scalar entrainment flux to the surface flux; i.e. $(\overline{w's'})_e / (\overline{w's'})_s$. Remember that $(\overline{w's'})_e = -w_e \Delta s$, which means that you need to initialise and probably adjust the scalar entrainment flux as a function of the entrainment velocity and the scalar jump at the free troposphere.

- **Experiment 7.3.2.** Number and name experiments: 1) *bottom-up*, 2) *top-down*, 3) *bottom-up-Advection*, 4) *bottom-up-Nadvection*, 5) *top-down-Advection* and 6) *top-down-Nadvection*.

Within the modelling framework of CLASS, advection of a scalar is prescribed as a constant external forcing within the ABL. For the experiments with positive advection, the scalar mixing ratio increases in both the *bottom-up* and *top-down* experiments, and *vice versa*. It is important to notice that advection has an impact on Δs and therefore on the entrainment flux (you can visualise this by plotting the entrainment flux of the scalar s $(\overline{w's'})_e$). In the experiments with positive advection of the scalar introduced in the ABL, the contribution of scalar advection tends at first to diminish the Δs and in some cases yields to a sign change of the entrainment flux: from a negative flux (scalar in the free troposphere is entrained into the

ABL) to a positive flux or upward flux (scalar is transported to the free troposphere). Similar behaviour can occur with negative scalar advection.

- **Experiment 7.3.3.** To further improve our quantification of the role of surface and entrainment processes, and the role of advection, we can calculate the budget of the scalar, *i.e.* the specific contribution of each process as a time-rate and therefore in units ppm s^{-1} . Figures AN5.1 and AN5.2 show the contribution of the various budgets to the scalar tendency (in ppb h^{-1}). The positive contribution of the surface is partly compensated for the entrainment of air with a low scalar mixing ratio. The larger entrainment effects occur in the first two hours of the run. As Figure AN5.1 shows, the tendency $\frac{\partial \langle s \rangle}{\partial t}$ remains positive throughout the experiment, which indicates that the scalar mixing ratio will increase during the experiment.

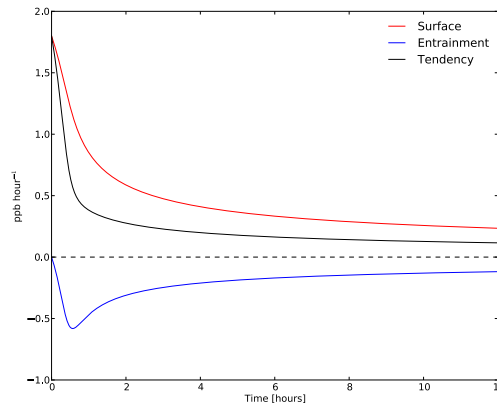


Figure AN5.1: Results of experiment 7.3.3 or budget study: Temporal evolution of the surface, entrainment and tendency contributions for the BOTTOM-UP without advection

The contribution of scalar advection to the budget of the scalar is shown in Figure AN5.2. Here, we show a case in which we impose a negative advection over the scalar constant on time ($-5 \cdot 10^{-5} \text{ ppm s}^{-1}$ or -0.18 ppm h^{-1}). The temporal evolution is very similar to that shown in Figure AN5.1, but in this case, the tendency term becomes slightly negative towards the end of the experiment. Also notice that, as previously mentioned, the contribution of entrainment is influenced by advection due to changes in Δs . You can observe this effect by comparing the contribution of entrainment in Figures AN5.1 and AN5.2. For the *advection* experiment, the entrainment contribution is less important for the scalar budget. For a fuller understanding of the combined role of surface, entrainment and advection processes, we recommend performing a sensitivity analysis using different rates of surface flux, free tropospheric conditions and scalar advection of the scalar.

- **Experiment 7.4.1.** Number and name experiments: 1) CO_2 -control, 2) CO_2 -uptake, 3) CO_2 -largergamma CO_2 , 4) CO_2 -subsidence and 5) CO_2 -advection.

This series of numerical experiments enables us to understand the effect of surface and external forcing on the carbon dioxide mixing ratio. We prescribe typical initial and boundary conditions observed in temperate climates covered by grass (more than 80 %) growing on a non-water stressed soil. Notice that in all the experiments, the off-line land surface modelling enables us to focus only on the effects of the surface and dynamics without taking the land-atmosphere interaction into account. In other words, the sensible, latent, and carbon

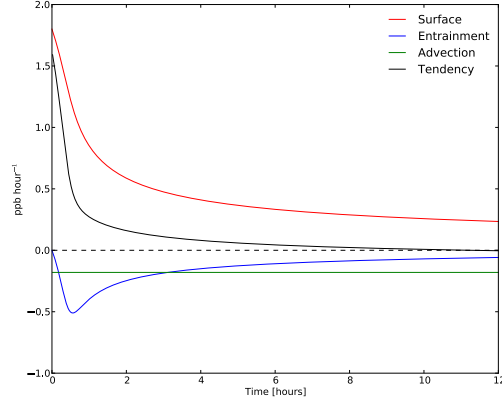


Figure AN5.2: Results of experiment 7.3.3 or budget study: Temporal evolution of the surface, entrainment and tendency for the BOTTOM-UP experiment with negative scalar advection. We prescribe a negative advection constant in time and equal to $-5 \cdot 10^{-5} \text{ ppb s}^{-1}$.

dioxide surface turbulent fluxes are all prescribed. It is important to stress that the dynamics of the ABL remains exactly the same in all the numerical experiments, apart from in the CO_2 -subsidence experiment that directly affects the ABL-dynamics. The main findings of the CO_2 -control experiment and the sensitivity analysis are summarised as follows:

1. Larger CO_2 assimilation uptake (experiment CO_2 -uptake). A larger negative flux of $(\overline{w'co_2'})_s$ results in a greater removal of carbon dioxide (see budget Equation 7.1) that leads to lower values of the CO_2 mixing ratio compared to the CONTROL case.
2. Larger γ_{CO_2} (CO_2 -largergamma CO_2). In this experiment, we find that if the mixing ratio of carbon dioxide is higher and changes with altitude in the free troposphere, the CO_2 within the ABL increases. The larger rise in CO_2 at the end of the experiment is due to the mixing ratio of carbon dioxide being larger at higher altitudes in the free troposphere. As an extension of this exercise, we can perform an additional experiment with a negative γ_{CO_2} and compare it to that in which the uptake of carbon dioxide is greater.
3. Larger subsidence (CO_2 -subsidence). This is the only experiment in which the dynamics change over time. As Equation 5.8 shows, subsidence limits the ability of the ABL to grow. In our experiment, we prescribe a divergence of the horizontal velocity equal to $2 \cdot 10^{-5} \text{ s}^{-1}$. As a result, the boundary layer grows until it reaches 800 m in the CO_2 -subsidence experiment compared to a maximum value at around 1200 m for the CO_2 -control experiment. The analysis of the CO_2 mixing ratio evolution can be counter-intuitive. A result of this difference in the height of the ABL, the shallow boundary layer leads to higher $\langle \text{CO}_2 \rangle$ since there is less volume in the ABL. However, the entrainment of CO_2 of poor air masses of carbon dioxide originated is larger (higher negative flux) that leads to lower CO_2 mixing ratio. In this case the latter effect is dominant and as a result, the experiment with SUBSIDENCE has lower CO_2 mixing ratio than the CONTROL case. The higher entrainment flux in the subsidence is explained by the higher entrainment velocities (you can plot w_e) (see Equation 4.5).
4. Positive advection of carbon dioxide (CO_2 -advection). A positive advection of carbon dioxide (for instance air masses originating in a city or industrial area and transported

towards the ABL) leads to a positive $\frac{\partial \text{CO}_2}{\partial t}$, thereby increasing the carbon dioxide mixing ratio with respect the dominant budget CO_2 ,

The numerical experiments of Chapter 12 complete the previous exercises and help us to understand the role played by an active plant physiology model in surface and boundary layer dynamics.

6

Answers Chapter 8

- **Experiment 8.3.1.1** Number and name experiments: 1) *chemistry-WI* and 2) *chemistry-SI*.

Dynamics. We begin by discussing the main differences in the dynamics of the *control-WI* and *control-SI* experiments. By plotting the ABL height h , we find that for the *SI* experiment the boundary layer height scarcely rises during the first two hours (from 200 m to 280 m). During this time, the mixed-layer potential temperature increases, because heat is distributed within a shallower boundary layer in the case of *control-SI* than in *control-WI*. The physical explanation of the delay of the ABL grow is that during the first two hours, the sensible heat flux introduced in the ABL is used to reduce the ground thermal inversion, as we can see by visualising the temporal evolution of $\Delta\theta$. In the course of the first two hours, the value decreases from 5 K to 1 K. Once this value has been reached, the boundary layer height starts to grow at a similar rate in the *control-WI* and *control-SI* experiments. However, the two-hours delay breaking the morning inversion yields to a final shallower boundary layer for the *SI* case compared to *control-WI*.

Chemistry. By plotting the temporal evolution of NO , NO_2 and O_3 we find that their evolution is constant through time (there is only a small adjustment of the mixing ratio of the three species to reach chemical equilibrium in the reactions R5 and R21, at the very beginning of the experiment), since for this simple numerical experiment, there are no emission or deposition fluxes, and the entrainment flux for the three species is zero because the jump of the mixing ratio between the free troposphere and the ABL for the three species is zero ($\Delta\text{O}_3 = \Delta\text{NO} = \Delta\text{NO}_2 = 0$ ppb). The photostationary state (Equation 8.5), which is equal to 1 for the whole run, confirms that the species are in chemical equilibrium and there is neither production nor destruction of the three chemically species. Finally, by filling out a EXCEL spreadsheet and calculating the chemically conserved species $\text{NO}_x = \text{NO} + \text{NO}_2$ and $\text{O}_x = \text{NO}_2 + \text{O}_3$, we find that the conserved variables for this triad species of this simple chemical mechanism are also constant through time.

- **Experiment 8.3.1.2** Number and name experiments: 1) *chemistry-WI/CASE1*, 2) *chemistry-highO₃/CASE2* and 3) *chemistry-lowO₃/CASE3*.

Using Figure 8.5 as a guide, we study the role of entrainment. In *CASE2*, the free tropospheric air masses are rich in ozone, implying that ozone produced in the stratosphere is transported downward, where it is entrained and leads to an increase in the O_3 mixing ratio within the ABL. Note that at the end of the *CASE2* experiment, the ozone mixing ratio tends towards the free tropospheric value (that is $\text{O}_{30} + \Delta\text{O}_{30}$). In *CASE3*, with a low O_3 mixing ratio in the free troposphere, we find that there is a drop in of the O_3 within the ABL due to entrainment of air, that is characterized by a low ozone mixing ratio. Consequently, $\text{O}_{3\text{ABL}}(t_{\text{final}}) \rightarrow \text{O}_{30} + \Delta\text{O}_{30}$.

- **Experiment 8.3.1.3** Number and name experiments: 1) *chemistry-clear/CONTROL*, 2) *chemistry-cloud* and 3) *chemistry-clear-winter*.

In this experiment, we focus on the role of NO_2 photolysis under different conditions of clear and cloudy skies. We take *CASE2* in the previous experiment 8.3.1.2. as a *CONTROL* case, and begin by plotting the photolysis rate NO_2 (reaction R5). The results show the clear relationship between radiation (UV) and the photolysis case. Under clear conditions, we obtain larger values. Under the totally overcast conditions (for instance in the presence of a homogeneous stratocumulus deck with cloud cover equal to 1), **photolysis rate** NO_2 has decreased by more than 50%. The reduction in **photolysis rate** NO_2 is even larger if instead of a summer day (Julian day=171), we perform the same calculations under midwinter day conditions (Julian day=355, experiment *chemistry clear-winter*).

As expected, by plotting temporal evolution of NO_2 , we find lower values for the clear experiment, due to the different photolysis rates in reaction 5. In turn, the higher photolysis rate leads to higher values of ozone and nitric oxide (reaction 23). The differences in O_3 are not very large (less than 0.5 ppb) but are in agreement with the different photolysis rates. By plotting the photostationary state, we find that only in the early morning and late afternoon the values are different from 1. During the remainder of the experiment, the species are continuously adjusted to a chemical equilibrium.

- **Experiment 8.3.2.1.** Number and name experiments: 1) *CASE1*, 2) *CASE2*, 3) *CASE3* and 4) *CASE4*.

We study four numerical experiments, gradually increasing the complexity of the chemical mechanisms involved. It is important to note that in all the experiments the dynamics of the ABL remain the same. You can check this by plotting the height of the boundary layer, the mixed-layer potential temperature and the mixed-layer specific moisture. We take *CASE2* of exercises 8.3.1.2 as a *CONTROL* case. In all the experiments, the photolysis rates of NO_2 (Reaction R5) and of O_3 (reaction R1) are constant over time. Figure AN6.1 shows the four experiments for the photostationary state, ozone, carbon monoxide and isoprene. Below, we discuss the more important features of the temporal evolution.

CASE1 has been previously discussed. Briefly, the three species (O_3 , NO and NO_2) are in chemical equilibrium. The increase in O_3 is therefore solely due to the entrainment of ozone that has originated in the free troposphere. In *CASE2*, we add four new reactions (R1, R2, R3 and R4). The photo dissociation reaction R1 destroys ozone, but it is produced again by reactions R3 and R4. The final effect is that a new chemical equilibrium is reached, but this time with slightly lower ozone values of around 30 ppb. For *CASE3*, the main effect of adding reactions R7 and R13 is the large rise in ozone in the first four hours of the simulation (see Figure AN6.1b). This is due to the major depletion of NO by reaction R13, due to the production of HO_2 by reaction R7. As Figure 8.4 shows, reaction R21 becomes less effective in destroying ozone and O_3 therefore increases. After four hours, CO is totally depleted (see Figure AN6.1c) and NO therefore increases, leading to a certain amount of destruction of ozone. Note that *CASE3* is unrealistic, since the atmospheric levels of CO are never close to zero with typical values of 100 ppb in less polluted areas, as we have described in most of the other numerical experiments.

Finally, *CASE4* represents the most realistic case, with the complex chemistry that leads to the formation of ozone by the combination of nitrogen compounds (NO and NO_2) with hydrocarbons (in our case represented by the generic hydrocarbon isoprene).

Figure 8.5 cancel **Figure 8.4** summarizes the main results for the four cases. Briefly, isoprene

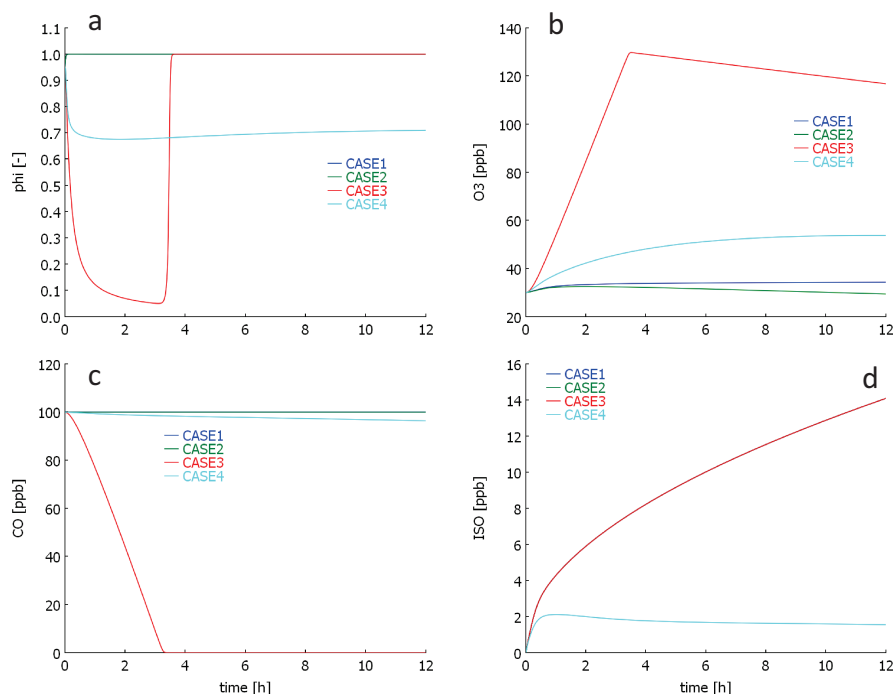


Figure AN6.1: Results of experiment 8.3.2.1: Temporal evolution of the photostationary state (a), ozone (b), carbon monoxide (c) and isoprene for the numerical experiments CASE1, 2, 3 and 4

and carbon dioxide reacting with OH produce HO_2 . NO_2 and HO_2 compete with each other to react with NO, with the result that NO decreases. As a result, the only reaction that destroys ozone (reaction 21) is limited by the amount of NO and the ozone mixing ratio therefore increases. Note that reactions R1-R4 are in near-equilibrium in the production/destruction of ozone. By introducing isoprene (representing generically the role of hydrocarbon) as a reactive species we find that it lowers the isoprene mixing rate in CASE 4, compared to CASES 1, 2 and 3, where isoprene acts as an inert species. Notice that in this case, the photolysis state is around 0.7, which indicates that ozone is being produced by the photolysis rate NO_2 .

- **Experiment 8.3.2.2.** Number and name experiments: 1) *complex*, 2) *complex-n=1*, 3) *complex-n=2*, 4) *complex-diurnal*, 5) *complex-n=1-diurnal* and 6) *complex-n=2-diurnal*.

Three experiments with constant (fixed) photolysis rate on time and emission of isoprene, and three with diurnal variation of the photolysis rate and emission of isoprene.

By including recycling in reaction R19 (extra production of OH by setting a stoichiometric coefficient n ranging between 1 and 2), we attempt to reproduce extra production of OH by other chemical pathways not explicitly included in the chemical mechanisms shown in Table 8.1. The main results for isoprene and OH are shown in Figure AN6.2. We performed two series of numerical experiments: the upper panel shows the results of isoprene and OH with constant photolysis rate and constant emission of isoprene, while the lower panel includes the diurnal evolution of the photolysis rate and the emission of isoprene by plants. This latter series of experiments is more realistic and is comparable to the conditions found in tropical rain-forests.

In the last three cases, we see that there is an increase of OH due to the larger emissions of

isoprene and NO. As a result reactions R9 and R15 yield a larger production of the radical RO_2 and HO_2 . In reaction R19, these both components are transformed producing OH (see figure 8.4). Ozone (not shown) is rather insensitive to recycling whereas HO_2 increases and MVK decreases. The rise in OH and other related chemical compounds enhances the oxidizing capacity of the atmosphere and permits the transformation of gases into products that are more easily removed by wet or dry deposition, *i.e.* the cleansing role of OH in the atmosphere.

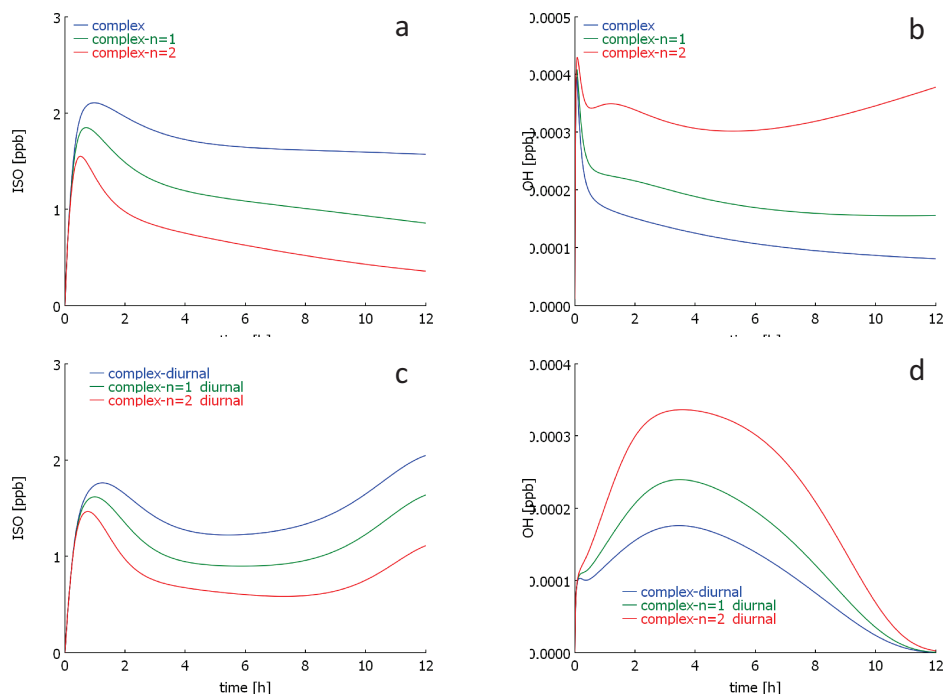


Figure AN6.2: Results of experiment 8.3.2.2: Temporal evolution of isoprene (a and c) and hydroxyl radical (b and d) to study the effect of OH recycling. In the numerical experiments (a) and (b) we prescribe a fixed photolysis rate and constant isoprene emissions. In the experiments shown in (c) and (d) we prescribe diurnal variations in the rate of photolysis and isoprene emissions

- **Experiment 8.3.2.3.** Number and name experiments: 1) *day-night* and 2) *day-nightdiurnalphoto*.

Experiment *day-night* has a constant (fixed) photolysis rate on time and experiment *day-nightdiurnalphoto* simulates a diurnal variation of the photolysis rate. By extending the integration time, we can gain a first impression of whether the other species in the chemical mechanism become more important under nocturnal conditions, *i.e.*, absence of photochemical reactions. As shown by the photolysis of NO_2 (using either a fixed or a diurnal value), after approximately 13 hours of the simulation, the NO_2 photodissociation rate becomes zero. At this point, other chemical species and reactions become more important. In particular, reactions R22 till R27, which involve the species NO_3 and N_2O_5 . By plotting these two reactants, we see that they are being produced under nocturnal conditions. Also note that they will act as a reservoir of the other nitrogen compounds, in particular NO and NO_2 . Nitrogen dioxide is still produced by the depletion of ozone by reaction R21, and therefore has higher mixing ratios than NO, which is almost totally depleted. Note that radical species such as OH and HO_2 approach mixing ratios close to zero during the night. It is important to remember

that in the morning, and as soon as the photochemical reactions begin to be activated by UV-radiation, NO_3 and N_2O_5 are destroyed, to produce NO and NO_2 .

- **Experiment 8.3.3.1.** Number and name experiments: 1) *chemistry-ml*, 2) *chemistry-polar* and 3) *chemistry-tropical*.

This series of numerical experiments completes exercise 4.2.1 (see section 4.2 for the discussion of the dynamics of the ABL). Here we study how different surface forcings (in this case represented only by the sensible heat flux) influence the evolution of ozone and other precursors by changing the dilution capacity of the ABL and the exchange of species between the ABL and FT. Larger h (in our case the *chemistry-tropical* experiment) leads to a higher entrainment rate (in our experiment $\text{O}_{3\text{FT}} > \text{O}_{3\text{ABL}}$) and therefore the $\text{O}_{3\text{ABL}}$ approaches the free tropospheric ratio at a much faster rate. The larger dilution caused by the increase in boundary layer growth under tropical conditions ($h_{\text{TROPICAL}} > h_{\text{MIDLAT}}$) partly counteracts this increase, but the larger entrainment is still the dominant process.

- **Experiment 8.3.3.2.** Number and name experiments: 1) *WI-lowNO*, 2) *SI-lowNO*, 3) *WI-highNO*, 4) *SI-highNO*, 5) *WI-lowNO-DiuEmis*, 6) *SI-lowNO-DiuEmis*, 7) *WI-highNO-DiuEmis* and 8) *SI-highNO-DiuEmis*.

The simple chemical mechanism enables us to understand a primary effect of the high emission of NO . As far as the numerical experiments under analysis are concerned, there are two main effects. The first is a general effect, since NO is not limited (NO is higher than 5 ppb), reaction R21 depletes ozone and ozone levels fall in all the experiments as NO emissions increase.

The second effect is related to the difference in the ozone levels due to the strengthening of the inversion (to observe this effect, compare the case of *SI* versus the *WI*). In the case of *SI*, NO accumulates during the early hours of the day before the morning inversion is broken, due to the shallower boundary layers (after four hours, simulation h is around 600 m for *WI* compared to 280 m for *SI*). This accumulation of NO leads to a high mixing ratio and therefore induces a depletion of ozone via reaction R21. This accumulation of NO can be quantified by plotting the NO mixing ratio and visualizing the NO morning peak and relating this to the temporal evolution of θ and $\Delta\theta$.

- **Experiment 8.3.3.3.** Number and name experiments: 1) *complex-WI*, 2) *complex-SI*, 3) *complex-WI-hFiso* 4) *complex-SI-hFiso*.

Switching on the complex mechanism yields a larger O_3 production. Figure 8.4 shows that the production of HO_2 via the reaction with isoprene (R9) and carbon monoxide (R7) and other compounds like the RO_2 radicals, leads to a destruction of NO . As a result, R21 is limited by the low NO mixing ratio that leads to rises in O_3 . In addition to this positive effect on ozone production, NO_2 is being formed by reactions R13, R14 and R15 yielding a larger production of O_3 by photodissociation.

In the case with strong inversion, we find that the precursors (for instance isoprene, CO) of HO_2 and RO_2 increase, due to the shallower boundary layers, and in consequence O_3 also increases. This increase can be partly offset by the higher NO mixing ratio in the case with strong inversion that contributes to a depletion of ozone via reaction R21.

- **Experiment 8.3.3.4.** Number and name experiments: 1) *complex-WI*, 2) *complex-SI*, 3) *complex-WI-urban* 4) *complex-SI-urban*.

First it is important to stress that now isoprene is acting as a generic hydrocarbon to mimic the more complex chemistry of urban areas. In these experiments under urban conditions (larger

emissions of NO and isoprene) we find the higher ozone mixing ratio. The explanation of the larger amount of ozone is similar to experiment 8.3.3.3, but now the chemical pathways in Figure 8.4 that connect OH with HO₂ and NO₂ are dominant and thus lead to a higher production of NO₂ and a limitation of NO production. The final outcome is the build-up of ozone to levels beyond 100 ppb.

- **Experiment 8.3.3.5.** We take the numerical experiment complex-WI as the main experiment and repeat it successively by changing the emissions of NO and isoprene.

We summarise the main findings of the sensitivity analysis to the emissions of NO and ISO in Figure AN6.3. We performed a series of numerical experiments with the same dynamic and chemistry conditions (minimum number of experiments was nine to get a first impression of the space parameter sensitivity), but modifying only the emissions of NO and isoprene. In Figure AN6.3, we show the final value of ozone at the end of the run time (12-hour time). Following Jacob (1999) as a guideline for the discussion, we distinguish two main regimes in Figure AN6.3:

1. Hydrocarbon-limited regime. This corresponds to the larger emissions of NO (higher than 0.5 ppb m s⁻¹) and low emission hydrocarbon. Under this regime, the ozone mixing ratio decreases due to reaction R21, and it therefore brings about a decrease in the ozone mixing ratio (46 ppb for the larger value of the emission of NO). A rise in hydrocarbon emissions (for instance in the experiments with emission levels of 0.5 ppb m s⁻¹ and 1.0 ppb m s⁻¹) increases the O₃ mixing ratio due to the formation of HO₂ and OH that form NO₂. NO₂ is a precursor of O₃ formation.

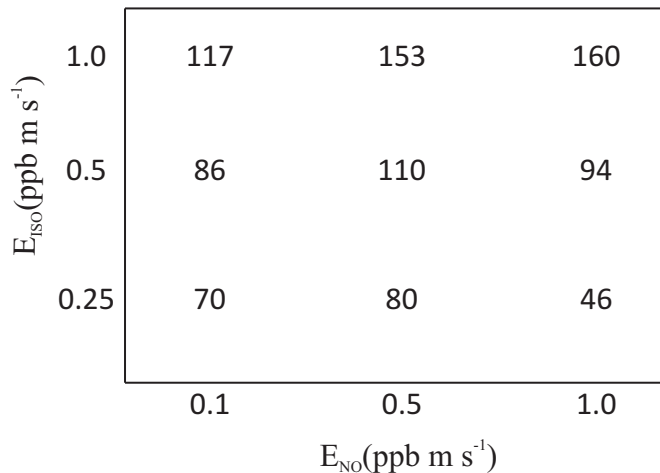


Figure AN6.3: Results of experiments 8.3.3.5: Values of ozone (in ppb) as a function of the initial emissions of nitric oxide and of isoprene. For all experiments, we show the value of O₃ mixing ratio at 12 UTC.

2. NO_x-limit regime. O₃ mixing ratios increase with hydrocarbon and NO_x emissions. This also demonstrates the non-linear dependence of O₃ on the emissions where doubling the emissions does not yield a doubling of the O₃ mixing ratio at the end of the simulation.

By performing more runs varying the emissions of NO and isoprene, we can complete Figure AN6.3 and draw a contour plot that will help to identify the NO-limiting and isoprene-limiting regimes.

Answers Chapter 10

- **Experiment 10.2.1.** Number and name experiments: 1) *CONTROL* and 2) *WET*.
Increasing soil moisture availability leads to an increase in the latent heat flux (LE). As shown by the moistening feedback (number 2 in Figure 10.1), this leads to a rise in specific moisture (see the arrow that connects $LE \rightarrow q$). Linked by the surface energy balance and as a result of the increase in LE , the sensible heat flux H falls, with a subsequent decrease in the boundary layer growth: see the connection $LE \rightarrow H \rightarrow h$ in Figure 10.1.

- **Experiment 10.3.1.** Number and name experiments: 1) *CONTROL*, 2) *CONTROL-highT*, 3) *CONTROL-noMXL* and 4) *CONTROL-highT-noMXL*.

In this experiment, we focus only on the effects of temperature on LE without taking the growth of the boundary layer into account. Note that we keep the ABL constant during the experiment, either by prescribing a very large jump in potential temperature (experiment *CONTROL*) or by switching off the mixed layer equations (experiment *CONTROL-noMXL*, this option can be found in the BASIC settings). Increasing the temperature θ_o leads to an enhancement of atmospheric water uptake capacity, and thus a rise in evaporation rate (see branch of the direct heating feedback loop $\theta \rightarrow LE$ in Figure 10.1).

It is important to note that the results differ, depending on the manner in which we prescribe the non-growth of the ABL. In the experiments in which we impose $\Delta\theta = 100$ K, the potential temperature also displays a diurnal variation that influences the sensible and latent heat fluxes. In contrast, in the experiments in which we switch off the mixed-layer equations, the potential temperature and other atmospheric variables remain constant and equal to the initial values. In other words, the atmosphere is treated as a reservoir and its atmospheric variables are not interacting with the surface processes.

- **Experiment 10.3.2.** Number and name experiments: 1) *CTRL*, 2) *CTRL-drier*, 3) *CTRL-noMXL* and 4) *CTRL-noNXL-drier*.

As in the previous experiment (no effects of ABL growth and no entrainment), a drier ABL leads to a rise in evaporation. Performing this experiment completes the moistening feedback explained in Figure 10.1, where an increase/decrease in q leads to a decrease/increase in LE . As in the previous experiment 10.3.1, we find different results when we reproduce the non-growth of the ABL by imposing a $\Delta\theta = 100$ K or switching off the atmospheric mixed-layer equations. In the former case, in spite of the boundary layer remaining constant over time, θ and q vary over time and are therefore influenced and coupled to the surface fluxes. This influence does not occur when we neglect the variation of atmospheric variables by decoupling these variables from the surface processes.

- **Experiment 10.4.1.** Number and name experiments: 1) *CONTROL* and 2) *CONTROL-drierFT*. This exercise is the first of a series of experiments on how evaporation and boundary layer clouds respond to different conditions at the inversion and in the free troposphere. Here, we compare the *CONTROL* experiment with an experiment designed to study the influence of drier air mass in the residual layer or free troposphere (for instance $\Delta q_o = -5 \text{ g}_w \text{ kg}_a^{-1}$). The results show that *LE* increases following the drying feedback at Figure 10.1). Under stress-free soils water conditions, dry air originating in the residual layer enhances *LE*. As a result, and because of the available energy the surface energy balance is equal, *H* diminishes and yields slower boundary layer growth. Therefore, the entrainment of dry air is also reduced, leading to a decrease in the entrainment of dry air. The complete loop is therefore a negative feedback loop in evaporation.

With respect to cloud formation, we find by plotting RH_{top} that the experiment with a drier residual layer leads to a drop in RH_{top} . As a result, the ABL thermodynamic conditions are less favourable to the formation of boundary-layer clouds.

- **Experiment 10.4.2.** Number and name experiments: 1) *CONTROL*, 2) *CONTROL-lowergT* and 3) *CONTROL-highergT*.

The lapse rate of potential temperature (γ_θ) controls boundary layer growth and is therefore an important external forcing factor in the determination of the height of the thermals. As we showed in Experiment 4.2.2, where lower γ_θ leads to a higher ABL, the absolute temperature falls facilitating the condensation process that can take place within the ABL. In the case of lower γ_θ , for instance $4 \cdot 10^{-3} \text{ K m}^{-1}$, the *h* is higher and the ABL conditions are therefore more favourable to the formation of boundary-layer clouds, since thermals reach altitudes that are characterized by lower absolute temperatures. Note that in this case, the mixed-layer temperature becomes colder, which has a negative impact on *LE* (see the direct heating feedback at Figure 10.1). Although this is the dominant effect, this decrease in *LE* is partly offset by the additional contribution of drying due to the enhancement of the entrainment process because of the deeper ABL.

- **Experiment 10.4.3.** Number and name experiments: 1) *CONTROL*, 2) *CONTROL-dryFT* and 3) *CONTROL-wetFT*.

As in Experiment 11.4.1, more negative γ_q will promote the drying of ABL. We can visualise this by plotting the temporal evolution of $\langle q \rangle$, which gives us a slight increase in *LE*, and the connection through the surface energy balance leads to lower *H*. Note that under stress-free soil-water conditions, free-tropospheric drying increases *LE* (see moistening feedback in Figure 10.1). Changes in γ_q have an impact on the temporal evolution of RH_{top} , which, decreases indicating a delay in, and fewer possibilities for cloud formation.

- **Experiment 10.5.1.** Number and name experiments: 1) *VEGETATION*, 2) *BARESOIL* and 3) *BARESOIL-albedo*.

We first analyze the differences between *VEGETATION* and *BARESOIL*. By plotting the soil moisture at the first level (volumetric water content top soil layer in graph CLASS), we find that vegetation regulates better the depletion of soil water compared to the case with bare soil. In spite of depleting less soil moisture, the latent heat flux becomes larger in the case of *VEGETATION* and it is also shifted its maximum. Therefore the presence of vegetation introduces a certain delay in the transport of water from the surface towards the atmosphere. This delay is regulated by the surface canopy resistance. Since the case has the same net available energy (plot Q_n), and in spite of the small differences in ground heat flux (plot *G*), the maximum sensible heat flux is a bit smaller in the numerical experiment *VEGETATION*

and therefore the boundary layer is in growth. This effect is partly offset when we reduce the albedo to 0.17 for the experiment *BARESOIL-albedo*. In that case, and as shown by the larger net available energy compared to *VEGETATION* and *BARESOIL*, H increase and we obtain the largest ABL-growth.

- **Experiment 10.6.1.** Number and name experiments: 1) *sandyloam*, 2) *sand*, 3) *clay* and 4) *sand-similarism*.

CLASS offer us the possibility to study how different soil types influence the boundary layer development. Note that although in this experiment we have reduced the vegetation cover (C_{veg}) to 50 % in order to study better the impact of different soil porosity and texture in the surface and atmospheric variables, vegetation still exerts an influence in our results. To have a complete understanding we design 4 different experiments: the first three have the same soil moisture index ($smi=0.256$), and the last one (*sand-similarism*) has the same absolute soil moisture content as *sandyloam* ($w_{soil1} = w_{soil2} = 0.21 \text{ m}^3 \text{ m}^{-3}$). First, we discuss how the different size and shape of soil pores yields to a different decrease in the soil moisture at the first level. Note that in this first experiments we prescribe an identical relative soil moisture by fixing the same soil moisture ($smi=0.256$) for the three experiments. We find that under *SAND* soil conditions, the soil moisture at level 1 is depleted faster due the largest pores (-28% decreased during the numerical experiment) The largest pores and texture favour the movement of water compared to clay characterized by the finest pores (-11% decrease). The combination and texture of *sandyloam* (less than 7% clay, less than 50 % silt and the rest sand) is the most effective in retaining water at the soil with a -6% decrease of the soil moisture content at level 1 and it provides rather efficiently water to the atmosphere under a series of negative conditions (compared to sand and clay). In that respect, *sandyloam* combines the best properties of clay to bind water and of sand characterized by larger pores enabling the drainage and the presence of oxygen.

Since in all the experiment the incoming shortwave radiation is identical and the longwave incoming and outgoing compensate each other, the net available energy Q_n introduced in the system is very similar (plot Q for the three soil types). The differences in the soil pores leads to a different partitioning in the surface energy balance. Comparing the soil types sand and *sandyloam*, we first find that the ground heat flux for the sand soil is the smallest due to the close values between the potential temperature in the atmosphere and the temperature in the first layer of the soil. Due to this low value of G , there is more energy available for the other heat fluxes. As a result, we find H has the higher values for sand. The latent heat flux is higher for *sandyloam* compared to sand, which can be related to the soil moisture at the first level. In contrast, the clay soil is the one with highest $Q_n - G$ and therefore the highest values for H . These higher values have direct consequences in the evolution of θ and q .

Taking into account boundary layer growth rate is highest in the clay case, we still find that in spite of being the large ABL the potential temperature values are the warmest for clay compared to the other cases due to high values of H for clay. In relation to the most optimal conditions for boundary-layer cloud formation, we find that in spite of obtaining the highest lifting condensation level, the experiment with *sandyloam* is the one with highest RH_{top} because the latent heat flux is highest as well.

The comparison of the results with identical absolute soil moisture, (*sandyloam* versus *sand-similarism*), is also interesting. The analysis of the soil moisture at the first level reveals that the soil characterized by coarser grain (sand) loses the soil moisture more rapidly than in the experiment *sandyloam*. Although the longwave incoming and outgoing radiation

have different evolutions, due to the different surface and atmospheric temperatures, they compensate each other, and as a result the available energy is almost similar. The results of the surface energy balance shows that the sand soils evaporate much more than the sandy loam. As a result, and due to the connection with the surface energy balance, the sensible heat flux is smaller in the *sand-similarity* than in the *sandyloam* experiment. This larger values for H of the sandy loam experiment yield the development of higher boundary layer characterized by warmer temperatures (large H and more entrainment of warm air) and drier conditions (lower LE and more entrainment of drier air).

- **Experiment 10.7.1.** Number and name experiments: 1) *CONTROL* and 2) *CONTROL-dew*.
The possibility of representing the evaporation of dew (or water that has been intercepted by the leaves) throughout Equation 9.21 offers interesting results. In contrast to transpiration through plants or soil processes, the water on the leaves is transferred very rapidly to the ABL. This is shown in the larger differences of LE between *CONTROL-dew* and *CONTROL*. In the first three hours of the morning transition LE (*CONTROL-dew*) is between 20-30 $W m^{-2}$ larger than in the numerical experiment without dew. Although the decrease in H is not as great, we find that *CONTROL* has a larger H and therefore will lead to the development of deeper ABL. The specific moisture is also larger in the case of dew. Note that because the evaporation occurs in the early hours of the day, when the boundary layer depth is shallower, the maximum value of q is much larger (approximately $0.2 g_w kg_a^{-1}$) than in the *CONTROL* experiment.

8

Answers Chapter 12

- **Experiment 12.1.1.** Number and name experiments: 1) *CONTROL*, 2) *WARMER* and 3) *WARMER-300*.

In order to ensure the consistency of the *WARMER* numerical experiment, it is necessary to ensure first that the initial soil temperature at the two levels is consistently prescribed with an additional 4 K and that the relative humidity at the surface is equal at the beginning of the simulations of the *CONTROL* and *WARMER* experiments.

For the sake of logical reasoning, we recommend plotting and discussing the following variables:

1. Surface (stomata) resistance. In spite of the rise in temperature between the *CONTROL* and *WARMER* experiments, the changes in the temporal evolution of r_s are very small. For a clearer sign of a reduction in the surface resistance, we need to initialise the model with a potential temperature above 300 K (experiment *WARMER-300*; 12 K more than the default value 288 K).
2. We now analyze the changes in the CO₂ budget due to alteration of photosynthesis assimilation, CO₂ soil respiration and surface energy balance. Remember that the latter can influence the boundary layer dynamics. By plotting first C_s (atmospheric mixed-layer carbon dioxide mixing ratio), we find that the atmospheric CO₂ is higher in the *WARMER* experiment (a difference of around 2 ppm). We therefore need to identify the reasons for the higher CO₂ mixing ratio in the *WARMER* experiment than the *CONTROL* experiment. There are three possible reasons, related to changes in the CO₂ surface fluxes or entrainment flux:
 - (a) Smaller photosynthesis assimilation rate in the numerical experiment *WARMER*. However by plotting wCO_2A , we find that the assimilation flux of CO₂ is almost identical. Therefore, the sensitivity of photosynthesis assimilation to global atmospheric warming is relatively minor.
 - (b) The *WARMER* experimental conditions lead to higher soil temperature and thus to a high CO₂ soil respiration rate (plot the variable wCO_2R in GRAPH). As a result, the net flux of CO₂, $\overline{(w'CO_2)'}_s$ (Equation 11.7), becomes smaller. In the CO₂-budget, this translates to a lower rate of decrease ~~rate~~ in the carbon dioxide mixing ratio (Equation 11.9).
 - (c) The *WARMER* experimental conditions also lead to an enhancement of the latent heat flux (larger capacity of the atmosphere in taking up water, see Figure 10.1).

As a result, the shifting of the energy balance partition towards LE leads to a fall in the sensible heat flux H in the *WARMER* experiment. Under these conditions, the boundary layer grows slowly and the entrainment velocity is reduced. As a result, the entrainment of free tropospheric air masses with lower CO_2 mixing ratio decreases, producing a even higher CO_2 mixing ratio within the ABL.

In conclusion, *WARMER* conditions lead to changes in the CO_2 -budget due to the enhancement of the CO_2 soil respiration (biological effect) and surface energy balance (including the carbon cycle variables), and therefore in ABL dynamics (physical effect).

- **Experiment 12.1.2.** Number and name experiments: 1) *CONTROL*, 2) *DrierSoil* ($W_{soil1} = W_{soil2} = 0.21 \text{ m}^3 \text{ m}^{-3}$), 3) *DrierFT* ($\Delta q = -5 \text{ gr kg}^{-1}$) and 4) *DrierSoil-FT* (combined both effects).

In this discussion, we follow a similar sequence as in the previous experiments.

1. Surface resistance. Plants react very strongly to water-stress (see Equation E.21). We find that r_s greatly increases (more than doubling) in the *DrierSoil* experiment, whereas the value of r_s is relatively unchanged in the *DrierFT* experiment compared to the *CONTROL* experiment.
2. Assimilation by photosynthesis. Larger r_s lead to a significant reduction in CO_2 uptake by the plant (more than 50 %). CO_2 soil respiration rates also increase under dry soil conditions. The combination of lower assimilation rate and higher soil respiration reduces (in absolute terms) the net exchange of carbon dioxide (surface kinematic flux $(\overline{w'c'})_s$) compared to the larger negative values in the *CONTROL* and *DrierFT* experiments. As a result, the decrease in temporal evolution of the the CO_2 -mixing ratio is more rapid in the case of *DrierSoil* than in the other two experiments.
3. Latent heat flux reacts differently from assimilation. The lower soil moisture considerably reduces evaporation. However, for the experiment with drier FT we find that the drying process driven by the entrainment of dry air from the free troposphere leads to higher rates of evaporation (see the drying feedback loop at Figure 10.1). By combining the two experiments (*Driersoil-FT*), we find that, in spite of the drying free troposphere feedback, LE still diminishes due to the reduced availability of soil moisture in the *Drier-soil* experiment. Remember that for the *Driersoil* experiment LE is limited by the amount of water within the soil.
4. Sensible heat flux will react to these changes in evaporation. Consequently, the highest sensible heat flux occurs for the *DrierSoil* experiment.

It is also in this case that the highest boundary-layer heights are obtained. In closing, it would be interesting to discuss the conditions under which the formation of boundary-layer clouds are optimal. In spite of the enhancement of LE , we find that the drying driven by entrainment leads to the lowest values of RH_{top} , and therefore to less favourable conditions for cloud formation.

- **Experiment 12.1.3.** Number and name experiments: 1) *CONTROL* and 2) *RISE-CO2*.

We compare here two experiments; *CONTROL* with CO_2 mixing ratio similar to the current levels, and *RISE-CO2*, in which we approximately double the CO_2 mixing ratio.

1. Surface (stomata) resistance and gross assimilation A_g . In the *RISE-CO2* experiment, we attempt to mimic the effect known as *carbon dioxide fertilization* (plants are more active and efficient in taking carbon dioxide due to the high atmospheric levels of CO_2). In the

RISE-CO2 experiment, we find that stomata resistance increases (low conductivity; see Equation E.18). We would expect that with larger r_s , the gross assimilation A_g (wCO2A) would become smaller in absolute terms. However, under the conditions of higher CO₂-mixing ratio, the rate of assimilation increases due to the high values of the CO₂ atmosphere mixing ratio. In short, the plant optimises its uptake by assimilating more CO₂ (steeper diffusion gradients between the plant and the atmosphere) and losing less water (see next point in this discussion).

2. Latent and sensible heat flux. By plotting LE , we find that the smaller surface resistance does indeed lead to a decrease in evaporation and thereafter an increase in the sensible heat flux. As a result, the boundary layer height increases. This makes it interesting to extend this discussion in order to determine how these surface forcing modifications affect cloud formation. On the one hand, in the *RISE-CO2* experiment, we find that the atmospheric moisture content decreases (less evaporation), which leads to a negative effect on cloud formation. On the other hand, the larger sensible heat flux leads to deeper boundary-layer clouds that enable the air parcel to reach a greater height at which the absolute temperature is lower. This effect favours boundary-layer formation. By visualizing RH_{top} , we find that in the *RISE-CO2* experiment there is a delay in RH_{top} in crossing the threshold 1 as an indicator of cloud formation (LCL also becomes higher). The *RISE-CO2* experiment thus shows that under conditions of rising carbon dioxide, boundary-layer clouds will have less favourable conditions due to the decreased latent heat flux.

– **Experiment 12.1.4.** Number and name experiments: 1) *CONTROL* and 2) *DIMMING*.

We study the effect of global dimming by lowering the value of incoming shortwave radiation (cloud cover 0.3; *DIMMING* experiment). Note that other important effects, associated with an increase in diffuse radiation from clouds, are not taken into account in this experiment. We follow a similar order as in the previous exercises:

1. Surface (stomata) resistance and gross assimilation A_g . In the *DIMMING* experiment, we find that the incoming shortwave radiation (plot this variable to ensure that your sensitivity analysis is correctly designed) decreases. The stomata/CO₂ gross assimilation are negative/postitive correlated to PAR (in our modelling framework we assume a very simplistic representation of PAR (see Equation E.19) up to saturation level (see Equations E.8 and E.18). As a result, the values of r_s and A_g are respectively higher and lower under global dimming conditions.
2. Latent and sensible heat flux. The reduction in r_s combined with the decrease in radiation result in the surface forcings falling between 10% and 30%. In other words, two of the most important components of the Penman-Monteith equation (Equation 9.16) contribute less to LE .
3. Boundary layer height and cloud formation. Due to the lower surface forcing (both in H and LE), the boundary layer height grows less and yields unfavourable conditions for the possibility of boundary-layer cloud formation (plot RH_{top} to visualize this): (1) less moisture in the atmosphere (2) thermals transporting heat and moisture are less strong and thus reach lower altitudes characterized by warmer conditions.

– **Experiment 12.1.5.** Number and name experiments: 1) *CONTROLC3* and 2) *CONTROLC4*. C4 plants are more effective than C3 in assimilating CO₂ and simultaneously losing less

water. In our CLASS modelling framework this is taken into account by prescribing different constants in the plant physiological model (see Table E.4). In order to make a fair comparison, in addition to substituting grass with maize (you can modify them in the settings SURFACE at the A-gs option), we recommend using the same vegetation conditions between grass and maize (in the settings ADVANCE SURFACE): *i.e.* same roughness length for momentum and heat, and same vegetation conditions in the ADVANCE SURFACE settings.

1. Surface (stomata) resistance and gross assimilation A_g . In the C4 numerical experiment, we find that the model represents higher stomata resistance, but the gross assimilation rates of the C4 plants are more extremely negative, indicating a greater uptake by these plants.
2. Latent heat and sensible heat flux. The opposite effects, to those of A_g , are found for the latent heat flux. The closing of the stomata enable the plant to lose less water by evaporation resulting in a significant reduction of LE for the *CONTROLC4* experiment. As a result, and connected by the surface energy balance relation, the sensible heat flux increases.
3. Boundary-layer height and cloud formation. Higher sensible heat flux leads to a deeper boundary-layer height that favours large-eddies or thermals reaching greater altitudes and therefore colder layers within the ABL (positive effect on cloud formation). However, the decrease in LE leads to a decrease in specific moisture $\langle q \rangle$ (negative effect on cloud formation). In comparing these two experiments, we find that relative humidity at the surface and at the top of the ABL is less for C4 plants than C3 plants. In consequence C3 plants and their subsequent influence on the surface fluxes are more favourable for an earlier formation of boundary-layer clouds.

Answers Chapter 13

- **Experiment 13.1.1.** Number and name experiments: 1) *NSB*, 2) *COLD*, 3) *WET* and 4) *SB*.

The advection of large-scale heat and moisture can have a profound impact on the development of the boundary layer dynamics and temporal evolution of the state variables. We performed the following four experiments: no sea breeze (*NSB*), advection of cold air (*COLD*), advection of moist air (*WET*) and sea breeze (*SB*). This enables us to learn systematically how the ABL responds to the advection of heat and moisture. We suggest analyzing the following variables:

1. Potential temperature and specific moisture. As expected, the advection of cold air leads to a significant decrease in the diurnal variability of potential temperature (check the lower values of $\langle\theta\rangle$) for the *COLD* and *SB* experiments. Similarly, moist advection increases the specific moisture during the day. Be sure to impose realistic values of heat and moisture advection.
2. Boundary layer height. The boundary layer height reacts differently to the advection of cold and moist air. It is in the *COLD* experiment that we find the shallowest boundary layer, compared to the deepest ABL height of the *WET* experiment. The reason for this is the different impact of advection in the sudden rise in virtual potential temperature ($\Delta\theta_v$) that enters explicitly into the calculation of boundary layer height (see Equation 5.8).

In the *COLD* case, we see that by plotting $\Delta\theta$ and $\Delta\theta_v$, both variables increase due to the decrease in $\langle\theta\rangle$ (see Equation 5.7). The advection of cold air thus reinforces the inversion at the top of the CBL that induce a stop in boundary layer growth. In turn, the advection of moist air produces an increase in the absolute value of the specific moisture (negative Δq) which in turn produces a fall in $\Delta\theta_v$. The latter can be physically interpreted as follows: an air parcel with identical momentum characteristics will have a greater density difference in the case characterized by drier free tropospheric air (for instance $\Delta q = -5 \text{ g kg}^{-1}$; denser) than one with moister conditions (for instances $\Delta q = -1 \text{ g kg}^{-1}$; lighter).

The end result is that in the *COLD* and *SB* experiments, we compute a larger $\Delta\theta_v$, which results in a stronger capping inversion and therefore a shallower boundary layer. It has been observed that sea breezes tend to stop boundary layer growth, in part due to the reinforcement of the capping inversion.

3. Cloud formation. The most favourable conditions for cloud formation depend on the absolute values prescribed for heat and moisture advection. In our case we prescribe

the following values: -0.72 K h^{-1} or -0.0002 K s^{-1} (heat) and $+0.72 \text{ (g kg}^{-1}) \text{ h}^{-1}$ or $0.0002 \text{ (g kg}^{-1}) \text{ s}^{-1}$ (moist). By plotting RH_{top} , we find that in spite of the shallower boundary layers, the *SB* experiment exhibits higher values, due to the colder mixed-layer potential temperature and the moister ABL. Both conditions favour the saturation process at lower heights.

- **Experiment 13.1.2.** Number and name experiments: 1) *SB-4hours*, 2) *SB-8hours*, 3) *SB-12hoursconstant* and 4) *NSB-12hoursconstant*

Here we discuss for the first time a numerical experiment that consists of two parts; After the first 4 hours the sea-breeze is entering (*SB-4hours*) and thereafter the sea-breeze is present for 8 hours(*SB-8hours*). The discussion in terms of the evolution of the potential temperature and specific humidity is very similar to that in the previous experiment. The interesting aspect is that this experiment can now quantify more realistically how the arrival of the sea breeze (in this specific case the sea breeze arrives four hours after starting the run) reinforces the capping inversion and slows ABL growth. To understand this effect, it is necessary to plot and analyze the evolution of $\Delta\theta_v$ (see the discussion of the previous experiment) and its sudden increase after four hours.

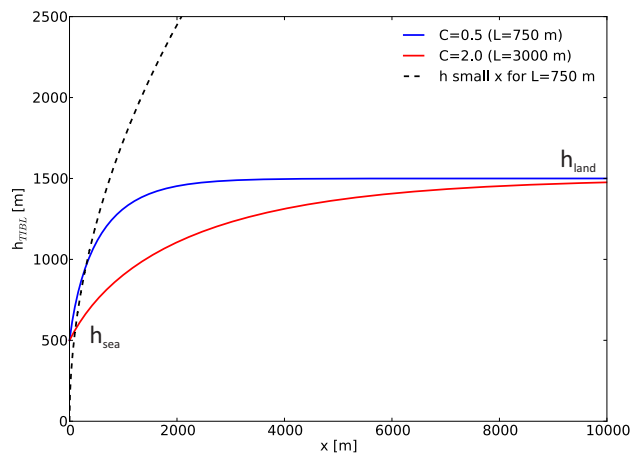


Figure AN9.1: Results of experiment 13.1.3: The boundary layer of the thermal internal boundary layer as a function of the distance x of shoreline. To calculate this we made use of Equation 13.5 using some typical values for the h_{LAND} (take a value for h from experiment 13.1.2) and h_{SEA} (for instance 500 m). In the figure we take $h_{\text{LAND}}=1500 \text{ m}$.

- **Experiment 13.1.3.** This exercise enable us to study the sensitivity in the development of the thermal internal boundary layer (TIBL) (Equation 13.5). And more specifically how TIBL varies with the distance from the coastline. Figure AN9.1 shows how the marine boundary layer h_{SEA} is advected and blends with h_{LAND} . The figure shows the relevance of the length scale to relaxation of the h_{LAND} , which is primarily driven by the surface forcing over land. In the case where $L = 300 \text{ m}$, the adjustment takes more than 10 kilometers whereas for $L = 750 \text{ m}$ the TIBL height becomes the h_{LAND} at only 2 km inland. These results also help us to put into perspective the previous experiments 13.1.1. and 13.1.2 where the TIBL was not taken into account and only the effect of advection of cold and moist air were studied with respect the ABL formation. Finally, the solution for shorter distance x near the shoreline shows that

$$h_{TIBL}^2 \sim (h_{LANDX}/C) \text{ (neglecting } h_{SEA}).$$

- **Experiment 13.2.1.** Number and name experiments: 1) *CONT-JS* and 2) *CONT-AGS*.

This five-day continuous experiment enables us to pinpoint the shortcomings of our modelling framework. And in particular the results obtained for integration times larger than the diurnal time-scale, including the formation and development of a nocturnal boundary layer. The most significant results of the experiment are shown in Figure AN9.2. In this figure time is plotted on the x-axis in h UTC to visualise the different runs after each other. We propose to visualise and discuss the following variables:

1. Radiation. Begin by checking four components of the radiation balance. The incoming and outgoing shortwave radiation are almost constant during the five days of the experiment, while the longwave components increase over time, due to the rise in temperature during the five-day event (see next points).
2. Soil moisture. As Figure AN9.2a shows, after a few days the soil moisture of level 1 reaches a steady state but it still oscillates. During the day the soil moisture decreases due to evaporation. During the night the soil moisture at level 1 gets refilled by the soil moisture from level 2. This is due to our assumption that soil moisture in layer 2 is constant over time and acts as an infinite reservoir of water (in our experiment $0.21 \text{ m}^3 \text{ m}^{-3}$).

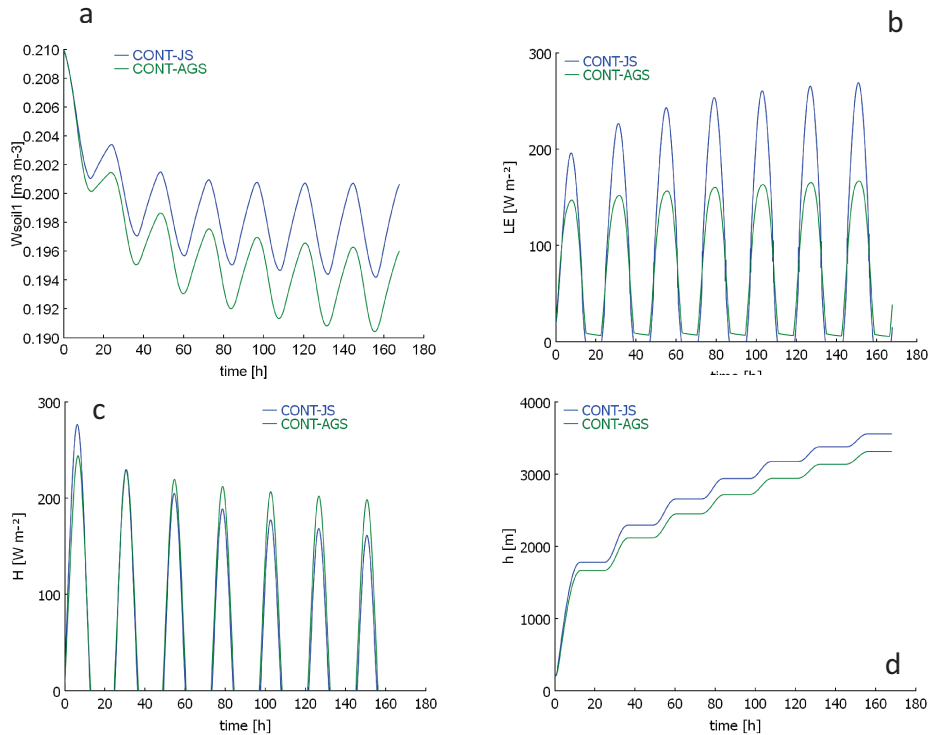


Figure AN9.2: Results of experiment 13.1.3: Temporal-evolution of soil moisture at level 1 (a), latent heat flux (b), sensible heat flux (c) and boundary layer height (d).

3. Surface forcing. During the multi-day drought event the latent heat flux increases (see Figure AN9.2b) and the sensible heat flux decreases (see Figure AN9.2c). LE may increase because soil moisture at level 2 is constant over time and ensures a constant supply of

soil moisture to level 1. The increase in LE is due to the higher temperatures (plot for instance the five-day mixed-layer potential temperature) that favours evaporation (see the feedback loop 1 related to *direct heating* in Figure 10.1). This is the same feedback loop that enables us to understand the corresponding decrease in the sensible heat flux (Figure AN9.2c).

It is interesting to study the effect of comparing a representation that includes feedback from plants (A-gs model) with another model that excludes such feedback (see Jarvis-Stewart representation in Chapter 9). As shown by the plots in Figures AN9.2b and AN9.2c, LE and H show similar trends. However, the evaporation is lower in the case of using the stomatal resistance modelled with A-gs representation. This is due to the stronger response of the surface (stomata) resistance to the decrease in soil moisture during the first day of the integration. By plotting r_s , we find that the values are higher, in particular for the first day, in the case of A-gs than in the Jarvis-Stewart model.

4. Boundary layer height. In this five-day continuous experiment, the boundary layer grows during the day and remains constant throughout the night (see Figure AN9.2d). In short, after the first day and night (approximately 26 hours after starting the run), the boundary layer will begin to grow at an unrealistic initial boundary layer height. This is due to the absence of formation of a nocturnal boundary layer: no thermal stratification due to longwave radiative cooling and therefore absence of removal of heat (you can visualise it by plotting potential temperature evolution). As a result the initial boundary layer height in day 2, day 3, day n begins with higher values of h_o . For example, using the Jarvis-Stewart option in the continuous experiment, we start at sunrise with higher initial boundary layer heights: $h_o=1660$ m (day 1); $h_o=2100$ m (day 2), and so on and so forth. In subsequent days, the boundary layer grows at lower rates (plot the entrainment velocity w_e to visualise it), with the following maximum values: 216 m h^{-1} or 0.06 m s^{-1} (day 1), 73 m h^{-1} or 0.02 m s^{-1} (day 2), 53 m h^{-1} or 0.014 m s^{-1} (day 3), 42 m h^{-1} or 0.011 m s^{-1} (day 4) and 31 m h^{-1} or 0.009 m s^{-1} (day 5). This is due to the continuous decrease in the sensible heat flux. It is important to stress the unrealistic evolution of h during the five-day event. In the following experiment, we attempt to improve this shortcoming by designing a non-continuous experiment on the multi-day drought event.

- **Experiment 13.2.2.** Number and name experiments: 1) *1day*, 2) *1night*, 3) *2day*, 4) *2night*, 5) *3day*, 6) *3night*, 7) *4day*, 8) *4night*, 9) *5day* and 10) *5night*.

We repeat the previous experiment but we design differently in order to take into account: (a) the decrease in soil moisture at the lowest level (level soil 2) and (b) the imposition of realistic conditions for h_o , θ_o and q_o . In doing so, we manually modify the soil moisture at level 2 and attempt to include the effect of night on the initial conditions. As explained in Section 13.2.2, we split the five-day drought into 10 different runs. Figure AN9.3 shows the main results.

1. Soil moisture at level 1. As Figure AN9.3a shows, soil moisture decreases during the day and remains constant throughout the night. Notice that in the experiment, we prescribe by default a 1% decrease at level 2 (see figure 13.5). A more accurate calculation can be performed by using expression 13.9. Save the output file and use an Excel spreadsheet or another software to calculate the expression. Using the evaporation values obtained in the first day of the drought (only during the day time conditions), and applying Equation 13.9, we find for a depth $L = 700$ mm that the depletion in the first day is equal to $-3.8 \cdot 10^{-3} \text{ m}^3 \text{ m}^{-3}$, *i.e.*, a -1.7 % decrease with respect to the initial value of $0.21 \cdot 10^{-3} \text{ m}^3 \text{ m}^{-3}$. Therefore our *ad-hoc* (first guess) estimate of 1% slightly underestimates this value.

Note that this value is highly dependent on the depths from which plants can take up water. At a smaller depth, $L = 300$ mm, we get a decrease of $-8.3 \cdot 10^{-3} \text{ m}^3 \text{ m}^{-3}$ (4% decrease). It is important to remind that we apply a constant decrease on time during the whole integration period. In reality, soil moisture decreases at a faster rate in the morning hours leading to a maximum LE that peaks earlier than the maximum of H .

At the end of the drought period, soil moisture at level 2 has fallen by 13 %. Comparing thus with Figure AN9.2a, the soil moisture shows a more realistic temporal evolution during the drought and we therefore obtain better results as regard to the radiation balance, the surface energy balance and the ABL dynamics. For the radiation balance, the four components present more realistic values and a clear separation of the diurnal and nocturnal variations.

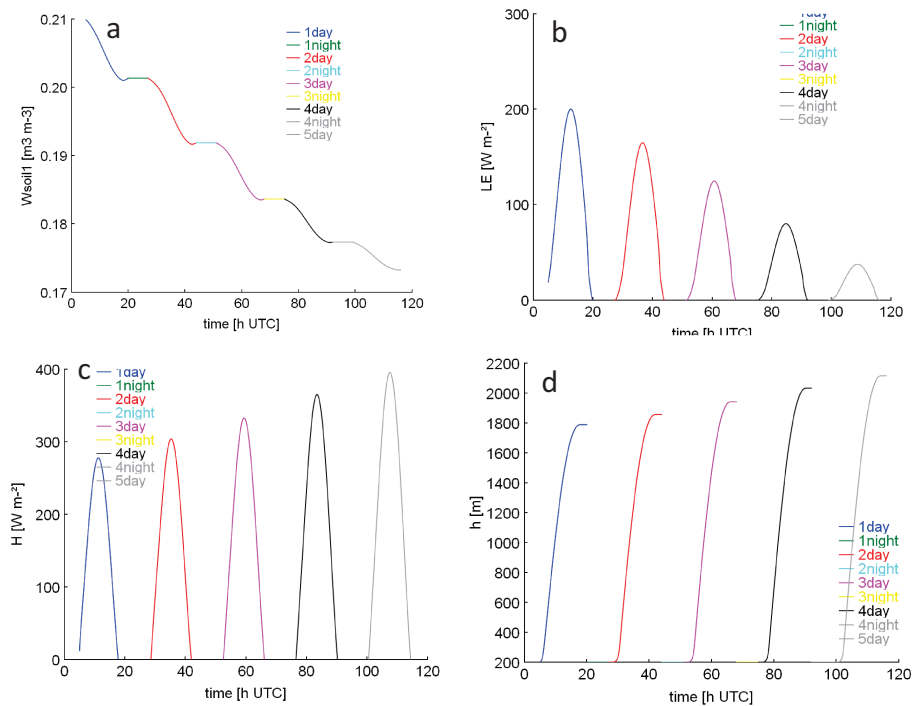


Figure AN9.3: Results of experiment 13.2.2: Five-days temporal-evolution of soil moisture at layer 1 (a), latent heat flux (b), sensible heat flux (c) and boundary layer height (d).

2. Surface forcings. Thanks to the more realistic temporal-evolution, we now obtain a drop in the latent heat flux (see Figure AN9.3b) and an increase in the sensible heat flux (see Figure AN9.3c). The reason is the imposed progressive reduction in the soil moisture content. For LE , the decrease during the drought period ranges between 30 and 40%. The increase in the sensible heat flux is slightly lower, at 10-20%.
3. Boundary-layer height and cloud formation. ABL height increases during the drought period from a maximum of 1780 m on day 1 to 1880 m on day 5, as a result of the increase in H . The temporal evolution of the surface forcing and ABL height also has consequences for the formation of boundary-layer clouds. By plotting RH_{top} , we find that there is a slight decrease in relative humidity at the top of the ABL, which can be explained by the fall in LE that is more dominant over the deeper ABL height (colder absolute temperatures) and therefore favourable conditions for a rise in RH_{top} .

- **Experiment 13.2.4.** By changing from grass to forest, we first found the differences in the absolute values of LE and H due to the larger surface resistance in forest compared to grass. As a result, we find higher/lower values of LE over grass/forest; and the other way around for the sensible heat flux. The ABL growth is therefore higher over the forest. Notice that certain conditions, such as albedo or roughness length, have also changed. However, the trend of the decrease in the drought is similar to that of grass.
- **Experiment 13.3.** Number and name experiments: 1) *1day*, 2) *1night*, 3) *2day*, 4) *2night*, 5) *3day*, 6) *3night*, 7) *4day*, 8) *4night*, 9) *5day* and 10) *5night*.

Figure AN9.4 shows the main results related to the accumulation of ozone during the 5 day air pollution event. The surface and dynamic processes have been discussed in the previous exercise. Due to the accumulation of ozone of the previous days, the maximum ozone values increases every day (Figure AN9.4a) under identical conditions of isoprene emissions (Figure AN9.4). Notice that the build-up of O_3 can be much larger if there is an increase in NO and hydrocarbon emissions, as studied in experiment 8.3.3.5.

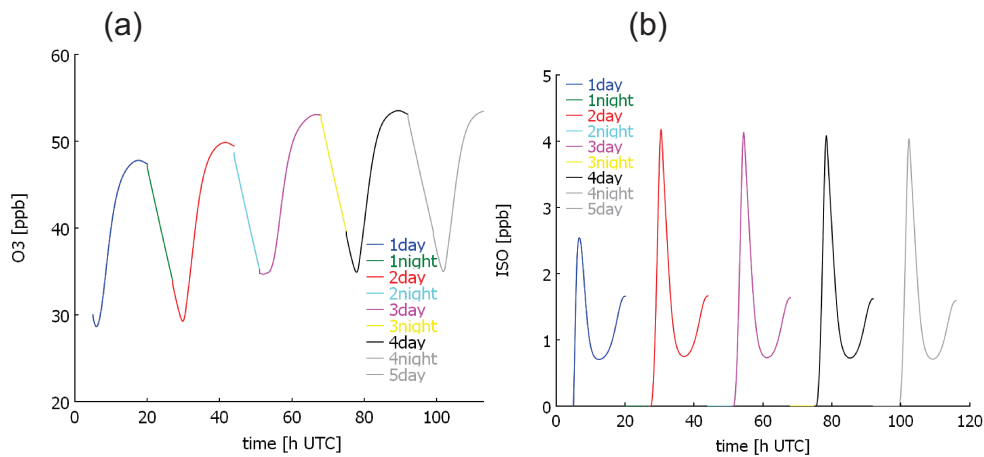


Figure AN9.4: Results of experiment 13.3: Temporal evolution of ozone (a) and isoprene (b) representing a 5-day air pollution event characterized by the build up of ozone.

10

Answers Chapter 14

- **Experiment 14.4.1.** Number and name experiments: 1) *lilly*, 2) *lilly(max ent)* and 3) *lilly(min ent)*.

Figure AN10.1 shows the vertical profiles of the potential temperature for the radiatively active dry smoke. The results are very similar to those obtained and discussed in the seminal research conducted by Lilly (1968). In short, the boundary layer grows as a result of the sea-surface sensible heat flux (first right-hand term in Equation 14.3) and the flux divergence of the longwave radiative cooling (last right-hand term in Equation 14.3). These two positive terms are compensated by the suppression of the ABL growth caused by the subsidence term (second right-hand term in Equation 14.3). The different values of the entrainment ratio for the virtual potential temperature (β) give slightly different values of the equilibrium value for h , but have an impact on the timing reaching the equilibrium. A higher entrainment rate leads to a shorter time to reach (steady-state) for the boundary layer height. After 120 hours of integration, we obtain the following values: for $\beta=1.0$, $h = 1836$ m; in the case that we prescribe $\beta=0.2$, $h = 1832$ m; in the case that $\beta=0.0$, $h = 1828$ m. At the end of the integration time, the mixed-layer potential temperature becomes equal to the sea-surface temperature that is equal to 285 K. You can visualise this by plotting the temporal evolution of the potential temperature. By this time, in all three experiments the ABL height (plot the temporal evolution) has reached a steady state, in which the entrainment driven by the longwave radiative cooling and subsidence are in balance.

- **Experiment 14.4.2.** Number and name experiments: 1) *sst285*, 2) *sst282* and 3) *sst288*.
By changing the values of the sea-surface temperature (for instance SST = 282 K or SST = 288 K), we find that the boundary layer reaches another equilibrium level. However, even for the case of SST 282 K (absence of surface sensible heat flux), a well-mixed ABL is formed. This is due to the longwave radiative cooling at its top (see Figure 14.5). Note also that this well-mixed boundary layer is capped by a strong potential temperature inversion jump that can be seen by plotting the temporal-evolution of $\Delta\theta$. Typical values of $\Delta\theta$ for a stratocumulus deck are higher than 5 K. In our experiments they range from 4.85 K (*sst288*) to 7 K (*sst282*). You can also check that the larger input of heat at sea level for the case *sst288* leads to higher potential temperatures in the mixed layer.
- **Experiment 14.4.3.** Number and name experiments: 1) *lat30N* and 2) *lat20N*.
By prescribing a smaller value of the divergence of the horizontal wind divergence (see Equation 4.4), e.g., $\text{div}U_h = 2.5 \cdot 10^{-6} \text{ s}^{-1}$ at the experiment *lat20N*, we find that a lower value of the subsidence leads to an increase in the equilibrium boundary layer height of the ABL.

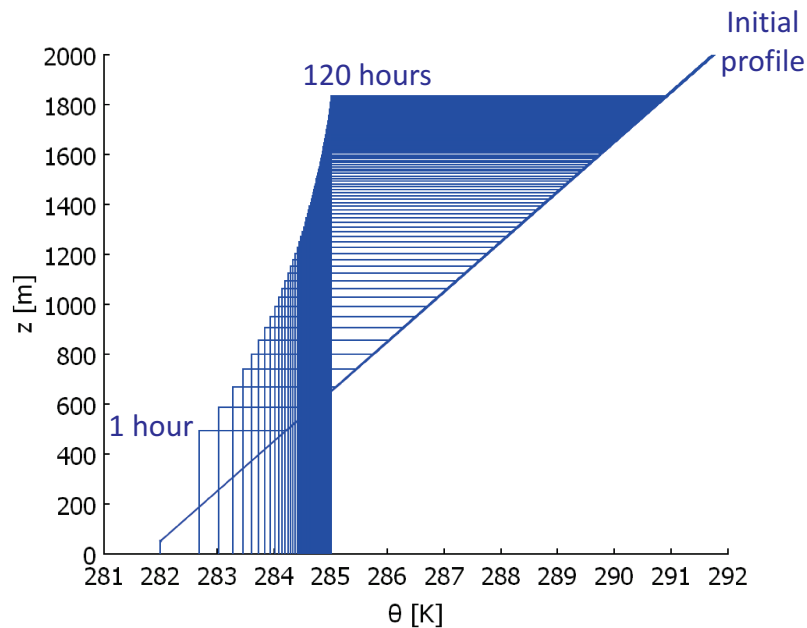


Figure AN10.1: Results of experiment 14.4.1: Time-dependent vertical profiles of the potential temperature of the dry cloud model for the case of $\beta = -0.2$ (experiment lilly). The diagonal line is the potential temperature initial profile characterized by a stable stratification almost reaching the sea surface. The vertical profiles of θ and q are similar to those presented in Figure 1 of [Lilly \(1968\)](#).

This experiment helps us to study the movement of the stratocumulus deck towards lower latitudes that eventually will lead to a breaking up of the deck and the formation of shallow cumulus. This transition from stratocumulus to shallow cumulus can also be accelerated (1) by the lowering of the potential temperature lapse rate (γ_θ) in the free troposphere, allowing a easier penetration of the parcels at higher altitudes and (2) by the rise in lower latitudes of the sea-surface temperature that leads to higher surface fluxes and therefore greater turbulence.

- **Experiment 14.4.4.** Number and name experiments: 1) *control72*, 2) *control36*, 3) *control10* and 4) *control00*.

A decrease in the divergence of the longwave radiation leads to a reduction in the main forcing of turbulence at the top of the CBL. As a result, the equilibrium of the ABL depth becomes lower. Notice, however, that the equilibrium potential temperature is the same, since it is determined by the sea-surface temperature

- **Experiment 14.4.5.** Although the previous experiments neglect the effect of phase changes, they have enabled us to introduce typical features of the marine boundary layer characterized by stratocumulus. Taking the control experiment as a reference case, we can also see that the sensible and latent heat flux decay with time until the mixed-layer temperature reaches the same value of SST. Another important feature is the absence of a diurnal variability in the temporal evolution of H and LE . The latent heat flux is the dominant surface forcing mechanism over the sea. You can check this by comparing the initial values of LE and H .

In our numerical experiments, the top of the cloud is given by the ABL height, which is characterized by a strong inversion. By analysing the RH_{surf} , we find that the stratocumulus will reach the sea surface after approximately 60 hours. In other words, the cloud base descends in the course of time, and the cloud occupies all of the ABL.

-
- **Experiment 14.4.6.** As a general discussion point to wrap up all the previous points, we need to stress: (1) the possibility of studying stratocumulus using the mixed-layer framework, (2) the relevance of the divergence of the longwave radiative cooling component in developing a mixed-layer over the sea, and (3) the importance of subsidence in controlling and forming an inversion layer. Moving towards lower latitudes will relax this last condition. As a result, more convective clouds such as shallow cumulus can form.

11

Answers Chapter 15

11.1 Section 15.2

Experiment 15.2. Number and name experiment: 1) *ABL-moistparcel*.

Here we provide a brief overview of the four exercises related to a moist air parcel that rises in the ABL and the vertical changes above and below the saturation point. Figures AN11.1 and AN11.2 show the main results of how the conserved and non-conserved variables related to temperature and moisture vary with height under the conditions summarised in Table 15.1. Note that in performing this analysis, we assume that the parcel is subject to the same initial conditions as at the start of the experiment: $\theta_p = \theta_o = 288$ K and $q_p = q_o = 8 \text{ g}_w \text{ kg}_a^{-1}$.

In Figure AN11.1a, the parcel rises, cooling adiabatically until it reaches a height of 560 m where due to its temperature and moisture conditions it reaches its saturation point, which marks the lifting condensation level LCL. This can be corroborated by Figure AN11.1b where RH becomes 100%. In Figure AN11.1a, we also show the temperature of the parcel (T_p). Above the LCL, and comparing T with T_p , we find that T_p is warmer because this temperature takes the release of latent heat due to condensation into account. As a result the air parcel will continue to rise after crossing the LCL.

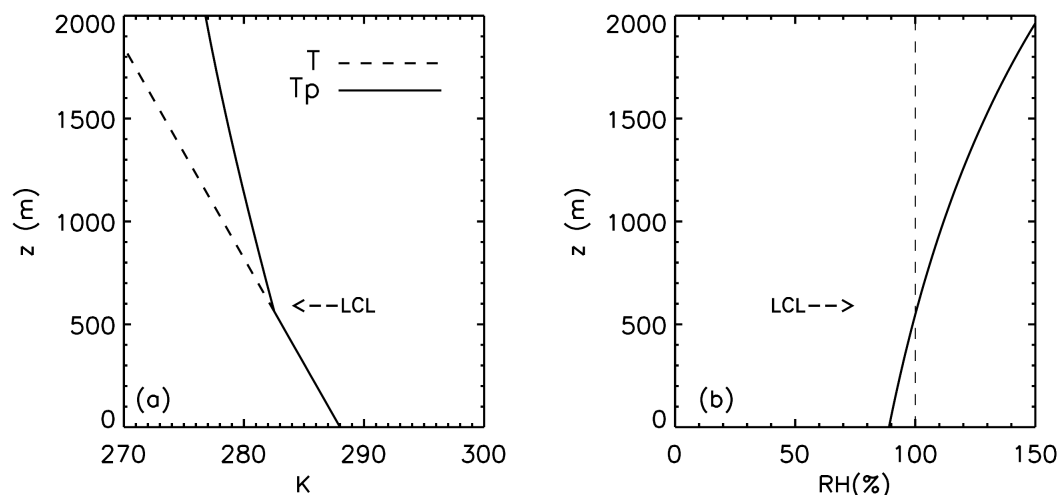


Figure AN11.1: Results of experiment 15.2: Vertical profiles of the absolute temperature and the temperature of the parcel (a). Relative humidity profile. LCL indicates the height of the lifting condensation level (b).

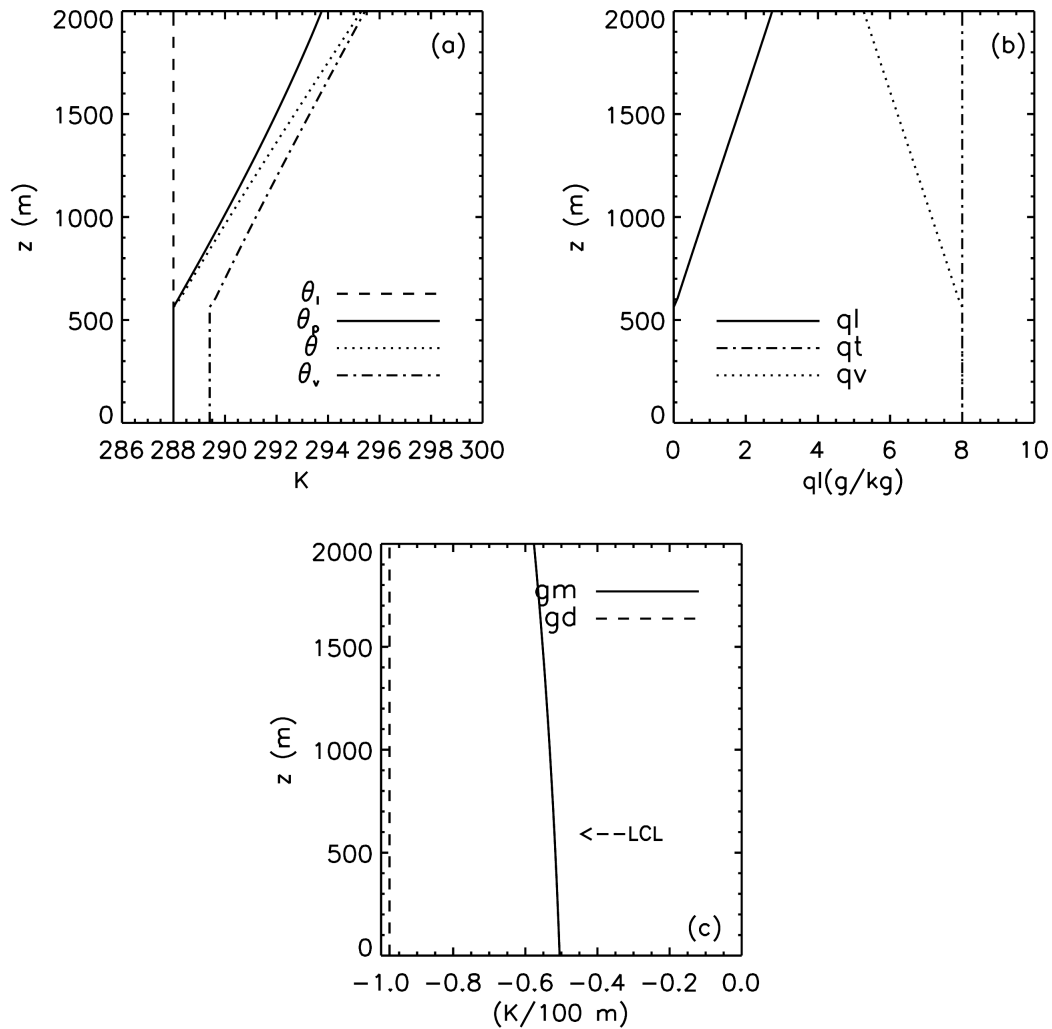


Figure AN11.2: Results of experiment 15.2: Vertical profiles of the liquid water potential temperature (θ_l), potential temperature environment (θ), potential temperature of the parcel (θ_p) and virtual potential temperature (θ_v) (a). Vertical profiles of the total specific humidity (q_t), vapour specific humidity (q_v) and liquid water (q_l) (see Box 8 for definitions) (b). Vertical profiles of the dry adiabatic lapse rate and moist adiabatic lapse rate calculated according to Equation 15.2 (c).

Figure AN11.2a shows the vertical profiles as a function of the different potential temperatures. The liquid water potential temperature (θ_l) is constant with height. This shows that it is conserved to two processes: (1) adiabatic cooling due to the upward movement (below and above LCL) and (2) release of heat due to phase changes (above LCL). The increase in the θ -values above LCL is due to the extra heat released by condensation. In calculating the potential temperature of the parcel θ_p that follows the moist adiabatic, we take the variations in the absolute temperature and the saturation specific moisture with height (Equation 15.2) into account. In the cloud layer, we find that the environment θ is smaller than the parcel potential temperature θ_p indicating that the parcel continues its ascent. This ascent will stop as soon as the parcel reaches an absolute inversion as shown by Figure 15.2. Finally, the virtual potential temperature shows a similar profile to θ , but now we take the contribution of the specific humidity into account, indicating that this is not a

conserved variable under conditions in which phase changes occur.

The conserved variable for the specific humidity is now q_t , with a profile that is constant with height. Above LCL, q_v decreases with height, since that part of the water vapour has condensed to liquid water (q_l). Notice that we calculated q_t as the difference between q_s and q_v . Finally, in Figure AN11.2c, we show quantitatively that the moist adiabatic lapse rate, is smaller in absolute terms than the dry adiabatic lapse rate due to the release of heat by condensation, *i.e.* values range from $-5 \cdot 10^{-3}$ to $-6 \cdot 10^{-3}$ K m⁻¹.

Note that throughout this exercise, we assume that variables such as potential temperature and specific humidity do not vary through time. In order to take this variation into account, we need to integrate the mixed-layer equations in time as is done by the model CLASS. We therefore recommend repeating the calculation for another point in time, when the ABL is already well-formed (for instance at 12 UTC). In particular, we can take the time when LCL becomes equal to h . We then expect that the calculation of LCL using the parcel method will be very similar to the one obtained using CLASS.

11.2 Section 15.5

- **Experiment 15.5.** Number and name experiments: 1) *ARM-noclouds*, 2) *ARM-scudyn*, 3) *ARM-scudyn-highLE* and 4) *ARM-scudyn-lowergq*.

The appearance of shallow cumulus in the ARM case (by switching on the parameterisation Shallow cumulus in the module radiation) has a noticeable effect on the main characteristics of the boundary-layer dynamics. As expressed by Equation 15.12, the boundary-layer height will grow less when the SCu are formed (at approximately 4.2 hours into the simulation, or 11 UTC). The mass flux associated with the shallow cumulus convection is responsible for this decrease. This shallower boundary layer leads to a rise in the potential temperature (around 0.5 K) because the heat is distributed within a smaller volume. We might expect to see similar behaviour from the specific moisture (rise in q due to the shallower ABL). However, the ventilation of q towards the cloud layer (see the last term on the right-hand side of Equation 15.11) becomes a dominant term. As a result, with the presence of clouds, the specific moisture will diminish over time, leading to drying of the sub-cloud layer. This process is a negative feedback in the formation and intensity of SCu.

As a discussion point, it is also important to notice that SCu are formed under average conditions of RH_{top} lower than 100 %. In that respect, the mass flux parameterisation included in CLASS satisfactorily reproduces the real conditions of shallow cumulus formation that are normally characterized by RH values that range between 80 and 90 %. This representation is therefore capable of mimicking the situation in which only thermals with sufficient vertical velocity and the necessary thermodynamic conditions will manage to reach the saturation point at the lifting condensation level. By visualising the cloud characteristics, we find values of the cloud core that range between 2% to 6%. Note that the cloud cores are the only positive buoyant components of the cloud and that this makes about 50 % of the cloud cover (normally ranges between 10-15%).

As the results of the sensitivity analysis suggest, higher values of LE will lead to an increase in cloud cover and mass flux, and subsequent variations in ABL dynamics. In turn, drying conditions in the free troposphere (for instance imposing a larger negative value of γ_q), leads to a fall in cloud and area cover, and the mass flux is lower.

- **Experiment 15.6.** Number and name experiments: 1) *ARM-nocl*, 2) *ARM-shcl*, 3) *ARM-shcl-*

rad, 4) *ARM-shcl-highsm* and 5) *ARM-shcl-lowgtheta*.

The presence of shallow cumulus influences the radiation and surface energy balances. In the case of radiation (option shallow cumulus Dynamics + radiation), we find that if shallow cumulus clouds are present the incoming shortwave radiation will decrease. Note that this decrease is less than 3 %. With respect to the latent heat flux, the drying of the ABL (around 8 gkg^{-1}) due to the appearance of clouds leads to a slight increase in the latent heat flux (see the temporal evolution of the experiment *ARM-shcl*, with the no radiation option). However, this increase is partly offset by the lower incoming shortwave radiation that leads to fall in *LE*. In all the cases the changes are less than 5% for all the key variables because of the relatively low cloud-cover values (less than 15% for SCu). For the boundary-layer dynamics and cloud characteristics, the results are similar to the previous experiment 15.5.

- **Experiment 15.7.** Number and name experiments: 1) *ARM-nocl-chem*, 2) *ARM-cld-chem*, 3) *ARM-nocl-chem-strO3*, 4) *ARM-cld-strO3* and 5) *ARM-cld-chem+rad*.

This experiment extends the effect of shallow cumulus to inert and reactive species in the sub-cloud layer. The dynamic aspects of the ARM numerical experiment have already been discussed. Shallow cumulus has two main effects on the chemistry: (1) a transport effect, by enhancing the ventilation from the sub-cloud layer into the cloud layer, and therefore removing compounds, (2) a reduction in dilution capacity, due to a slowing down of the ABL growth and therefore less entrainment (Equation 5.13) and (3) disturbance of the photodissociation rate by decreasing its values.

Focusing first on the dynamic effects, we find that both inert scalars and reactants (for instance ozone, nitric oxide and isoprene) fall during shallow cumulus convection (in the ARM case, clouds appear four hours after the start of the experiment). This negative effect of the mixing ratio is more important than the effect of shallower ABL height, which reduces the dilution capacity of the ABL. In air-pollution studies, this effect is known as "ventilation".

Finally, the photolysis rate is affected by clouds. This can be checked by plotting the photolysis of NO_2 . There is only a reduction of the photolysis rate visible for the experiment *ARM-cld-chem+rad*, as in this experiment the radiation option for shallow cumulus is switched on and therefore lead to a decrease of the photolysis rate. The effect on ozone is minimal due to the reduced cloud cover (less than 10%). It is important to stress that due to the simplicity of our representation of clouds, we calculate an average decrease in the photodissociation rate. In more detailed calculations, including a more realistic representation of the clouds, the photolysis of NO_2 (k_{r05}) or other photodissociated reactants, is more affected by clouds. The changes are larger in the vertical profile of k_{r05} above, with linear decreases in and below the cloud.

Bibliography

Jacob DJ (1999) Introduction to atmospheric chemistry, Princeton University Press, p 266

Lilly DK (1968) Models of cloud-topped mixed layers under a strong inversion. *Quart J Roy Meteorol Soc* 94:292–309

Schröter J, Moene AF, Holtslag AAM (2013) Convective boundary layer wind dynamics and inertial oscillations: the influence of surface stress. *Quart J Roy Meteorol Soc* 135:1277–1291